JGR Oceans

RESEARCH ARTICLE
10.1029/2021JC018315

Dispersion Processes in Weakly Dissipative Tidal Channels

A. De Leo[1], N. Tambroni[1], and A. Stocchino[2]

[1]Dipartimento di Ingegneria Civile, Chimica e Ambientale, Università degli Studi di Genova, Genova, Italy, [2]Department of Civil and Environmental Engineering, Hong Kong Polytechnic University, Kowloon, Hong Kong

Key Points:

- A large-scale physical model is used to study tidal dispersion and the flood-macrovortices generated at the inlet
- The Lagrangian integral scale and the corresponding dispersion coefficients attain a constant value for increasing friction parameter
- Dispersion processes are dominated by local dynamics for particle separations larger than the typical tidal inlet length scale

Supporting Information:

Supporting Information may be found in the online version of this article.

Correspondence to:

A. De Leo, and A. Stocchino,
annalisa.deleo@edu.unige.it;
alessandro.stocchino@polyu.edu.hk

Citation:

De Leo, A., Tambroni, N., & Stocchino, A. (2022). Dispersion processes in weakly dissipative tidal channels. *Journal of Geophysical Research: Oceans*, *127*, e2021JC018315. https://doi.org/10.1029/2021JC018315

Received 3 DEC 2021
Accepted 1 OCT 2022

Author Contributions:

Conceptualization: A. De Leo, N. Tambroni, A. Stocchino
Data curation: A. De Leo, A. Stocchino
Formal analysis: A. De Leo, N. Tambroni, A. Stocchino
Investigation: A. De Leo, N. Tambroni, A. Stocchino
Methodology: A. De Leo, N. Tambroni, A. Stocchino
Supervision: N. Tambroni, A. Stocchino
Visualization: A. De Leo
Writing – original draft: N. Tambroni, A. Stocchino
Writing – review & editing: A. De Leo, N. Tambroni, A. Stocchino

Abstract We report the results of an extensive experimental campaign dedicated to the analysis of turbulent dispersion owing to the circulations in tidal environments, characterized by a tidal inlet and a channel with lateral tidal flats. We focus on weakly-convergent and weakly-dissipative estuaries or tidal embankments, where the internal waters communicate with the open sea through an inlet mouth. Tides are reproduced as single or multiple harmonics waves. Particle Image Velocimetry is employed to measure two-dimensional surface velocity fields. Large-scale macro-vortices, generated by vortex shedding during the flood phase from the inlet barrier, tend to occupy the entire tidal flats width and are completely flushed out during the ebb phase. In all experiments, an intense residual current, with shape influenced by the large-scale flood vortices, is observed. The presence of large-scale vortices and of a residual current strongly influences the Lagrangian auto-correlation functions and the corresponding absolute dispersion time evolution. Looping auto-correlations are the signature of both periodic forcing and vortices, ultimately, leading to super diffusive regimes. An asymptotic Brownian regime is always found for the investigated range of parameters allowing for an estimate of the horizontal dispersion coefficients which turn out to decrease with the friction parameter and tend to be enhanced when the semi-diurnal constituents prevail. Finally, multiple particle statistics show multiple regimes depending on particle separations, compared to a typical injection length scale that seems to coincide with the inlet mouth dimension.

Plain Language Summary Estuaries are unique environments where inland water carried by rivers meets salty sea water. The encounter of masses of water with different characteristics (chemical composition, temperature, etc.) makes estuaries extremely dynamic environments suitable for the proliferation of a great variety of ecosystems and biodiversities. In this work, we investigate the dispersion processes using a large-scale physical model of a simple geometry estuary, bounded by an inlet mouth, where tides are the dominant drivers. We aim to analyze the dispersion regimes relying on two-dimensional velocity measurements at the free surface as a basis for a Lagrangian analysis. We show how the presence of a tidal inlet generates complex flow patterns depending on the forcing tides. The resulting residual current is the main responsible for a net longitudinal dispersion that can be characterized by high values of the corresponding dispersion coefficients. Moreover, the mixed character of the tides may play an important role on the dispersion processes, enhancing the ability of the flow to transport mass in the main flow direction.

1. Introduction

Estuaries are considered transitional regions between landward waters and open sea, and thus important sites for human development. Estuarine regions can be classified depending on morphology, geometry configurations, vertical salinity stratification, and finally hydrodynamics (Valle-Levinson, 2010). In particular, coastal bays and estuaries are characterized by flows driven by hydraulic unbalance such as baroclinic pressure gradients, river inflows and wind stresses, and tidal waves. In a recent contribution, Valle-Levinson (2021) proposed a classification based on the dynamical balance between different mechanical drivers (tides and density gradients) in particular for semienclosed basins.

If on one hand, tidal propagation has been deeply studied in order to better understand the suitable parameters to describe them (Cai et al., 2012; Seminara et al., 2010; Toffolon et al., 2006), on the other hand, the role of tides on mass transport still requires a thorough investigation. The role of tidal circulation in estuarine mixing was considered of less importance for several decades (Geyer & MacCready, 2014). However, the so-called residual currents derived by averaging over a tidal period are recognized to be a fundamental driver for mass transport and dispersion processes (Jay, 1991; Zimmerman, 1986) owing to the strong and persistent straining and shearing (Ridderinkhof & Zimmerman, 1992). The time periodic character of the tides also generates dispersion

mechanisms sustained by different flow scales especially if related to the complex geometry of real estuaries, tidal embankments, or coastal lagoons. The presence of a tidal inlet can, for example, generate macro-vortices that during a tidal cycle may influence the momentum and mass transport on relatively large distances (Awaji, 1982; Awaji et al., 1980; Branyon et al., 2022).

Several studies focused on the definition of the time scales and the estimation of the dispersion coefficients in monochromatic tidal force conditions (see Cucco et al., 2009; Umgiesser et al., 2014; Viero & Defina, 2016, among others). At the same time, several works were dedicated to the prediction of multi-harmonic tides (Amin, 1986; Lee & Chang, 2019) and their propagation (Cai et al., 2012; Fortunato & Oliveira, 2005; Jay, 1991; Seminara et al., 2010; Toffolon et al., 2006). However, the investigation of the effects of multiple harmonics on the flow field and dispersion processes lacks of evidence. In fact, field studies devoted to estimation of longitudinal dispersion coefficients (Banas et al., 2004; Lewis & Uncles, 2003; Monismith et al., 2002) did not provide any relationship among the coefficients and the tidal wave shapes. Several field measurements of longitudinal dispersion coefficient reported a wide range of values, spanning almost two order of magnitudes from 10 to 10^3 m^2/s^{-1} (Banas et al., 2004; Fischer et al., 1979; Lewis & Uncles, 2003; Monismith et al., 2002). Moreover, tides tend to produce non-monotonic particle velocity correlation leading to possible particle looping trajectories that also reflect on a looping character of the Lagrangian integral time scales, differently from the classical statistically steady or homogeneous turbulence (Enrile et al., 2019). Looping-like particle trajectories have been also studied in oceanic context and they were found to be related to particular dispersion regimes (Berloff et al., 2002; Enrile et al., 2019; Veneziani et al., 2004).

Two of the main issues concern with the definition of typical transport time scales, relevant for dispersion and water quality problems and for the estimate of the dispersion coefficients that control longitudinal transport. Seeking a reliable definition of the time scale for transport processes led to use different measures such as residence time, flushing time, age (see Cucco et al., 2009; Umgiesser et al., 2014; Viero & Defina, 2016; Yang et al., 2018 among many others). The attempt was to classify estuaries based on these time scales and an example can be found in Umgiesser et al. (2014) where several estuaries and coastal bays of the Mediterranean Sea were compared. However, most of these time scales were based on Eulerian concepts and quite a few on Lagrangian approaches.

Classical analyses in terms of single and multiple particle statistics are very seldom applied to estuaries compared to oceanographic and atmospheric applications (LaCasce, 2008). Moreover, attempts to study the dispersion processes under controlled laboratory conditions in simplified estuaries are very limited in literature (Dronkers, 2019; Kusumoto, 2008; Nicolau del Roure et al., 2009), although worth pursuing. Indeed, controlled experiments with simple boundary conditions provide a measure of some of the main mechanisms that drive the dispersion process, a goal quite difficult to achieve on the basis of field observations whose interpretation is generally complicated by the large scale of the processes, more irregular natural geometries and the simultaneous presence of a variety of features whose role cannot be readily isolated. Moreover, they provide a useful dataset to test reliability of analytical and numerical models.

In the present study, we aim to investigate the relevant dispersion processes using a large-scale physical model of a weakly-dissipative tide dominated estuary (Cai et al., 2012; Toffolon et al., 2006) characterized by the presence of an inlet mouth that connects the outer sea to a compound tidal channel. Flow is forced by tidal variation imposed at the outer basin. In an attempt to understand the role of the tidal constituents, we designed this study with the aim to firstly investigate the role of a single harmonic and secondly the role of two harmonics, representing the semi-diurnal and diurnal components, with different tidal form factor. We provide a detailed description of the transient macro-vortices generated at the inlet and the resulting residual current for the different tidal forcings. The generation of flood-vortices is compared with previous works (Nicolau del Roure et al., 2009) and extended considering the effect of the vorticity generation owing to the depth jump between the channel and the tidal flats (Brocchini & Colombini, 2004; Stocchino et al., 2011). Large-scale Particle Image Velocimetry is employed to measure 2D surface velocity fields providing a high spatial and temporal description of the flow. A detailed Lagrangian analysis of the typical integral scales and of single and multiple particle statistics, varying the controlling parameter, is performed and provides a clearer picture of the processes occurring in weakly-dissipative estuaries.

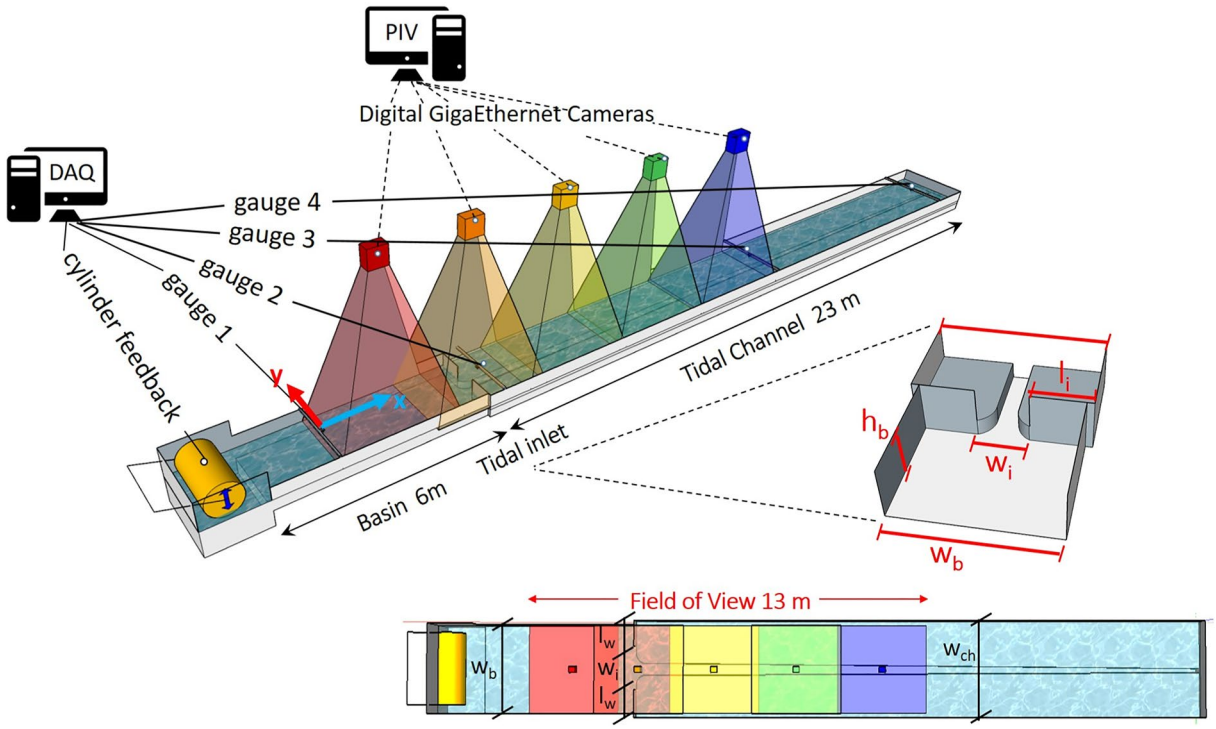

Figure 1. Sketch of the experimental setup and measuring systems: 3D view, detail of the tidal inlet and top-view panel.

Finally, the flow structures at different scales generated by the interaction of the tidal wave with the inlet mouth are expected to be further complicated by increasing the complexity of the tidal waves, with possible effects on the main dispersion processes. To assess the interplay of the flow structures at different scales and the resulting dispersion regimes, multiple particle statistics have proven to be an effective analysis when applied to geophysical flows (LaCasce, 2008; Orre et al., 2006). In fact, the theoretical results in terms of relative dispersion and Finite Size Lyapunov Exponents suggest the possible existence of local and nonlocal dynamical behaviors (Babiano et al., 1990; Bennett, 1984; Kraichnan, 1966; Lin, 1972). The latter regimes are associated to particle separations that are influenced by different flow scales. Applications to geophysical flows showed the existence of both regimes when the flow is mainly generated by the tides (Enrile et al., 2019). In the present study, we will perform multiple particle statistics based on the measured flow fields generated by both a single harmonic and multiple harmonics tides.

2. Experimental Set-Up and Measuring Techniques

The experiments were performed in a physical model in the hydraulic Laboratory of the Department of Civil, Chemical and Environmental Engineering of the University of Genova, Italy. A sketch of the overall experimental setup is shown in Figure 1. The experimental apparatus consists of a tidal channel, closed at one end and connected to a rectangular basin, representing the sea, at the other end. The tidal channel (23 m long) is characterized by a symmetrical compound cross-section with a deep main channel and lateral flats with an overall width equal to w_{ch} = 2.42 m. The main channel has a 2.5‰ longitudinal slope and a rectangular cross-section with a landward decreasing width, starting from about 70 cm at the tidal inlet (w_i), reaching about 11 cm at the channel end. Consequently, the two tidal flats have a varying width between 0.86 and 1.16 m on each side. The elevation of the tidal flats relative to the bottom of the main channel is constant and equal to 0.24 m. The basin is 6 m long and 2.20 m wide (w_b), with side walls height equal to h_b = 0.5 m. Contrary to the tidal channel, the bottom of the basin is horizontal. Tidal flats are closed at the inlet through two thin vertical plates (l_i = 0.86 m) which separate them from the outer sea-basin. Hence water exchange between the basin and the channel is allowed only at the inlet cross-section of the main tidal channel.

The present experiments have been performed keeping a constant mean water depth equal to 0.36 m at the channel inlet. The estimate of the conductance coefficient C is about 12, which corresponds to a Manning's resistance coefficient of about 0.0167 $sm^{-1/3}$.

Tides have been reproduced by imposing regular volume waves with variable period and amplitude, generated by the periodic motion of an oscillating cylinder inside an adjacent feeding tank. To minimize wave reflections, a dissipative sloping mound was installed at the end of the channel. The cylinder is remotely controlled through a digital signal acquisition-generation system and its motion provides a free surface elevation η at the channel inlet that, in the most general formulation, reads:

$$\eta(t) = \sum_i a_i \sin(\omega_i t + \phi_i) \tag{1}$$

where t is the time, a_i is the amplitude, ϕ_i is the phase shift, and $\omega_i = 2\pi/T_i$ the tidal angular frequency of the ith tidal component, being T_i the tidal period. In the following, we take advantage of this general formulation in order to distinguish between *single* component tides and *multiple* components tides.

The first set of experiments were performed forcing the tidal channel with a series of single harmonic tides of the kind $\eta(t) = a \sin(\omega t)$. In particular, we considered five different amplitudes a for four tidal periods T, resulting in a total of 20 experiments.

The second series of experiments, for a total of 19 runs, were designed with the aim to understand the role of multiple constituents of the tidal forcing signal, mimicking a more realistic tidal wave. Therefore, we imposed a simplified form for the astronomical tidal free surface oscillation that reads:

$$\eta(t) = a_{sd} \sin(\omega_{sd} t) + a_d \sin\left(\frac{\omega_{sd}}{2} t + \phi\right) \tag{2}$$

where a_{sd} and a_d represent the amplitude of a *semidiurnal* and *diurnal* component, respectively, and ω_{sd} is the angular frequency of the *semidiurnal* component. We consider that the *diurnal* component has a period doubled with respect to the *semidiurnal* one.

The relative importance of the semi-diurnal and diurnal components can be expressed through the form factor F defined as (Lee & Chang, 2019):

$$F = \frac{a_d}{a_{sd}} \tag{3}$$

The form parameter can be used to discriminate the different types of astronomical tide, in particular:

- if $F < 0.25$, the tide is semi-diurnal;
- if $0.25 < F < 1.25$, the tide is mixed, but mainly semi-diurnal;
- if $1.25 < F < 3.0$, the tide is mixed, but mainly diurnal;
- if $F > 3.0$, the tide is diurnal.

In the present study, we varied the form factor F in a range between 0.08 and 1.6 (see Table 1), which well represents a variety of realistic situations (Tsimplis et al., 1995).

Moreover, the phase shift introduced in Equation 2 has been varied to understand the role of the phase lag between the semi-diurnal and diurnal constituents on the tidal wave shape. To this end, for a fixed value of F, we imposed three values of the phase shift ϕ, namely $-\pi/4$, 0, and $\pi/4$.

During each experiment, water level and surface velocities were measured. In particular, free surface elevation was monitored using four ultrasound gauges (Honeywell model 946-A4V-2D-2C0-380E, with 30 cm range and an accuracy of 0.2% of the full scale), placed on the axis of the channel respectively at a distance of 0, 4.75, 14.3, and 25 m from the wave maker (see Figure 1). Large Scale Particle Image Velocimetry (LS-PIV) was employed to measure the 2D time-dependent free surface velocity fields $\mathbf{u}(x, y, t) = (u(x, y, t), v(x, y, t))$, where, according to the notations of Figure 1, we denote by x the landward oriented longitudinal axis of the channel with origin located in the basin at a distance of 3 m from the channel inlet and by y the lateral coordinate; u and v are the x and y components of the velocity $\mathbf{u}$, respectively. It is worth noting that, the large dimension of the interested area imposes specific equipment modifications to the standard PIV technique. The channel water surface was densely

Table 1
Main Experimental Parameters and External Parameters as Reported in Toffolon et al. (2006)

		Exp.	a [m]	R_h [m]	T [s]	R_e	χ	γ
Single component series		08-SC	0.0010	0.086	160	9485	0.010	1.02
		09-SC	0.0037	0.086	160	20,923	0.08	1.02
		10-SC	0.0055	0.086	160	25,845	0.12	1.02
		11-SC	0.0081	0.086	160	29,981	0.18	1.02
		12-SC	0.0093	0.086	160	35,902	0.21	1.02
		13-SC	0.0013	0.086	100	17,881	0.02	0.64
		14-SC	0.0026	0.086	100	30,853	0.04	0.64
		15-SC	0.0044	0.086	100	33,837	0.06	0.64
		16-SC	0.0076	0.086	100	30,984	0.10	0.64
		17-SC	0.0118	0.086	100	43,470	0.16	0.64
		18-SC	0.0013	0.086	130	13,783	0.02	0.83
		19-SC	0.0027	0.086	130	23,452	0.05	0.83
		20-SC	0.0044	0.086	130	30,541	0.08	0.83
		21-SC	0.0062	0.086	130	36,422	0.11	0.83
		22-SC	0.0079	0.086	130	44,764	0.14	0.83
		23-SC	0.002	0.086	180	8172	0.05	1.15
		24-SC	0.0039	0.086	180	15,930	0.10	1.15
		25-SC	0.0055	0.086	180	14,287	0.14	1.15
		26-SC	0.0076	0.086	180	27,268	0.19	1.15
		27-SC	0.0091	0.086	180	35,195	0.23	1.15
		Exp.	a_{sd} [m]	a_d [m]	T_{sd} [s]	T_d [s]	ϕ	F
Multi components series	Series 1	01-MC	0.017	0.0015	100	200	0	0.08
		02-MC	0.013	0.003	100	200	0	0.2
		03-MC	0.013	0.0035	100	200	0	0.3
		04-MC	0.012	0.0046	100	200	0	0.4
		05-MC	0.0075	0.006	100	200	0	0.8
		06-MC	0.006	0.007	100	200	0	1.2
		07-MC	0.005	0.008	100	200	0	1.6
	Series 2	08-MC	0.013	0.003	100	200	$-\phi/4$	0.2
		09-MC	0.013	0.0035	100	200	$-\phi/4$	0.3
		10-MC	0.012	0.0046	100	200	$-\phi/4$	0.4
		11-MC	0.0075	0.006	100	200	$-\phi/4$	0.8
		12-MC	0.006	0.007	100	200	$-\phi/4$	1.2
		13-MC	0.005	0.008	100	200	$-\phi/4$	1.6
	Series 3	14-MC	0.013	0.003	100	200	$\phi/4$	0.2
		15-MC	0.013	0.0035	100	200	$\phi/4$	0.3
		16-MC	0.012	0.0046	100	200	$\phi/4$	0.4
		17-MC	0.0075	0.006	100	200	$\phi/4$	0.8
		18-MC	0.006	0.007	100	200	$\phi/4$	1.2
		19-MC	0.005	0.008	100	200	$\phi/4$	1.6

Note. SC refers to the single component cases and MC to the multi components series of experiments. For the single component experiments, seven preliminary runs were performed just with the aim to tune the PIV system whereby they are not reported in the table.

and uniformly seeded by polyethylene particles (940 kg m^{-3}, mean dimension 3 mm) used as PIV tracers. LS-PIV acquisitions were recorded employing five high-resolution GigaEthernet digital camera (Teledyne Dalsa Genie Nano C1280 and C2450). Depending on the camera model, the resolutions varied between 2448 × 2048 pixels and 1280 × 1024 pixels. A 6-mm lens have been mounted on the cameras. Cameras were fixed on rigid supports placed at an elevation of 4 m from the bottom of the channel, pointing downwards, as shown in Figure 1. Based on the camera arrangement, the field of view (FoV) for the velocity measurements was set such to cover a large area of about 13 × 2 m, extending from about the last 3 m of the basin to about the first 10 m of the channel for the entire width, with cameras overlapping in the longitudinal direction of about 20%. Lighting was produced using eight 500 W white light halogen lamps. The LS-PIV acquisition frame rate was set equal to 10 fps. A single acquisition lasted for about five tidal periods and, thus, each camera recorded between 5,000 and 13,000 images, depending on the experimental parameters. The images from the five digital cameras have, then, been processed in order to obtain a single panoramic image of the entire FoV before PIV analysis, performed using the software proVision-XS^{TM} (Integrated Design Tools Inc).

3. Data Processing and Background on Lagrangian Mixing

3.1. Eulerian Analysis

The superficial 2D Eulerian velocity fields $\mathbf{u}(\mathbf{x}, t)$ are the result of PIV analysis. First, the Eulerian fields have been post-processed with the aim to distinguish regions with different dynamical properties and identify vortical structures at different scales. Among the many techniques of vortex identification, we employed the method based on the evaluation of the Okubo-Weiss parameter (Okubo, 1970; Weiss, 1991). For steady or slowly time-dependent flows, the Okubo-Weiss criterion makes use of the eigenvalues of the local velocity gradient tensor $\mathbf{D}$, which can be written as $\mathbf{D}^2 = \lambda_0 \mathbf{I}$, where the Okubo-Weiss parameter $\lambda_0 = -\det(\mathbf{D})$ is the product of the eigenvalues of $\mathbf{D}$. It may be appropriate to write λ_0 in the form suggested by Weiss (1991), that is, $\lambda_0 = \frac{1}{4}\left(S^2 - \omega^2\right)$ where $S^2 = S_n^2 + S_s^2$ is the total square strain, sum of the normal ($S_n = \partial u/\partial x - \partial v/\partial y$) and shear ($S_s = \partial v/\partial x + \partial u/\partial y$) components, and ω^2 is the square vorticity ($\omega = \partial v/\partial x - \partial u/\partial y$). Note that, since we are dealing with 2D velocity fields, the only component of the vorticity vector is the out-of-plane one. The sign of λ_0 discriminates between locally hyperbolic flow regions ($\lambda_0 > 0$ strain dominated) and locally elliptical flow regions ($\lambda_0 < 0$ rotation dominated). The latter are signature of coherent vortices. For the present analysis we are mostly interested to identify the presence of coherent vortices at different scales and during the flow dynamic in a tidal cycle.

3.2. Lagrangian Analysis

The most natural framework for analyzing mixing processes is the Lagrangian (or material) one, which studies the evolution of material particles during the flow motion. To this end, we started from the Eulerian velocity fields ($\mathbf{u}(\mathbf{x}, t)$) and computed the numerical trajectories of material particles by integrating $\dot{\mathbf{x}}(t) = \mathbf{u}(\mathbf{x}, t)$ using a fourth-order Runge-Kutta algorithm with adaptive step size. About 2×10^4 trajectories have been computed, from a regular grid seeding over a 10 × 2 m representing the entire measure domain.

The numerical particle trajectories are then employed to estimate single and multiple particle statistics (LaCasce, 2008). In particular, we define the absolute dispersion $\mathbf{A}^2(t)$ and its trace, the total absolute dispersion $a^2(t)$, as (Elhmaïdi et al., 1993; LaCasce, 2008; Provenzale, 1999; Stocchino et al., 2011):

$$A_{ij}^2(t) = \frac{1}{M}\sum_{m=1}^{M}\left\{\left[x_i^m(t) - x_i^m(t_0)\right]\left[x_j^m(t) - x_j^m(t_0)\right]\right\} \qquad a^2(t) = \mathrm{Tr}(\mathbf{A}) \tag{4}$$

where M is the number of particles and $\mathbf{x}^m(t)$ is the position of the mth particle at time t and $\mathbf{x}^m(t_0)$ its initial position. Note that the time derivative of $a^2(t)$ provides an estimate of the total absolute diffusivity coefficient $K(t)$ (LaCasce, 2008; Provenzale, 1999). Classical dispersion regimes are identified based on the time dependence of the total absolute dispersion following the theory of Taylor (1921), found to be valid in several geophysical contexts (LaCasce, 2008). The so-called Lagrangian integral scale T_L separates the quadratic and the linear time

dependence regime of the absolute dispersion. It is defined as the time integral of the Lagrangian autocorrelation function of the ith Lagrangian velocity component u_{L_i}:

$$T_{L_i} = \int_0^{+\infty} \mathcal{R}_{ii} d\tau \qquad \mathcal{R}_{ii}(\tau) = \frac{1}{M} \sum_M \frac{\rho_{L_{ii}}(\tau)}{\sqrt{\rho_{L_{ii}}(0)^2}} \qquad \rho_{L_{ii}}(\tau) = \langle u_{L_i}(t) u_{L_i}(t+\tau) \rangle. \tag{5}$$

where the brackets indicate an average over the entire duration of each trajectory. The Lagrangian integral time scale T_L is then calculated as the average of the longitudinal and transverse time scale, namely $T_L = 1/2(T_{Lx} + T_{Ly})$.

Differently from the single particle statistics, multiple-particle statistics or relative dispersion aim to study the separation of couples of particles in time, providing insight of the interplay among the different flow scales. The relative dispersion matrix $\boldsymbol{R}^2(r_0, t)$ is defined as the mean-square distance at time t between a pair of particles that at time t_0 had a distance equal to r_0:

$$R_{ij}^2(r_0, t) = \frac{1}{M-1} \sum_{m=1}^{M-1} \left\{ \left[x_i^m(t) - x_i^{m+1}(t) \right] \left[x_j^m(t) - x_j^{m+1}(t) \right] \right\} \tag{6}$$

where $M-1$ is the number of particle pairs initially at distant r_0. As for the total absolute dispersion a^2, the total relative dispersion $r^2(t)$ is simply the trace of the relative dispersion matrix $\boldsymbol{R}^2(r_0, t)$ and the total relative diffusivity $D(t)$ is its time derivative. Together with the relative dispersion, we employ another Lagrangian measure commonly used in dispersion studies, namely the Finite Scale Lyapunov Exponents Λ (FSLE). FSLEs consist in averaging the times required to particle pairs to separate from an initial distance to a final one (see Artale et al., 1997; Cencini & Vulpiani, 2013; LaCasce, 2008, among others). Thus, in order to calculate the FSLE, it is necessary to first choose a set of distances that are recursively increased as:

$$r_n = \delta r_{n-1} = \delta^n r_0, \tag{7}$$

where n is the chosen number of separation and δ is an arbitrary constant larger than unity. The second step consists in calculating the times (known as "exit time" T_n) required for each pair displacement to grow to the following r_n. At each distance the maximum FSLE is computed as:

$$\Lambda(r) = \frac{1}{\langle T_n \rangle} \log(\delta), \tag{8}$$

where the brackets indicate an ensemble average over the particle pairs that effectively reach the r_n distance. Care must be taken in the choice of the multiplier δ in order to correctly capture the regimes of the flow at hand (Haza et al., 2008). In our experiments, we set $\delta = 1.2$ as in Enrile et al. (2019). Both relative dispersion and FSLE have been extensively used in oceanographic and coastal studies leading to a better comprehension of the physical processes at the different separation scales (Artale et al., 1997; Enrile, Besio, Stocchino, Magaldi, et al., 2018; Enrile et al., 2019; Haza et al., 2008; LaCasce, 2008; Orre et al., 2006).

4. Scaling Arguments and Estuary Classification

Dealing with large-scale geophysical problems, such as hydrodynamics and mixing processes in estuaries, tidal embankments, or small coastal bays/lagoons, poses several challenges especially when the approach is based on laboratory experiments. The typical dimensions of these natural aquatic environments are usually of the order of several kilometers in the longitudinal and, possibly, in the transversal direction, and of several meters along the vertical. Thus, a proper scaling is necessary in order to avoid spurious effects owing to the small scale of the laboratory facilities compared with the prototypes.

In this section, we focus our attention on two main aspects: which is the correct similitude to adopt and to what extent our measurements are relatable to realistic contexts. Regarding the similitude, it is of paramount importance to firstly define which physical parameters are relevant to our process. The definition of the correct dimensionless parameters for the hydrodynamic behavior of estuaries was long debated in the literature. Several attempts to find simple scaling of the main processes were presented by Jay (1991), Savenije (1993) and Lanzoni and Seminara (1998) among others.

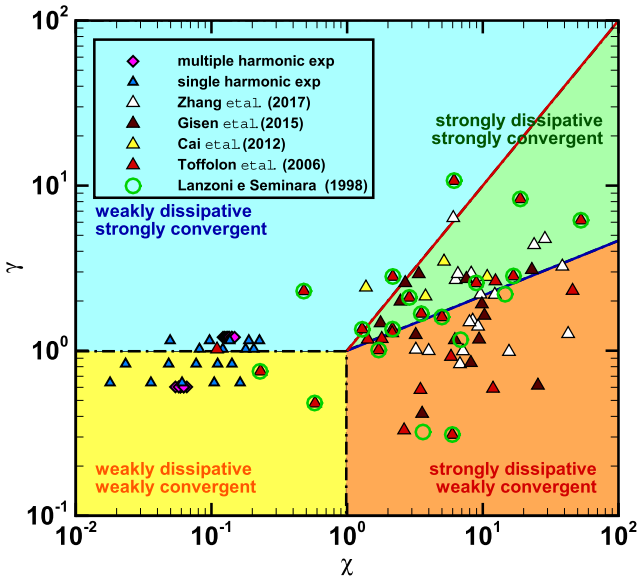

Figure 2. (χ, γ)-plane classification of several natural estuaries as reported in Lanzoni and Seminara (1998), Toffolon et al. (2006), Cai et al. (2012), Gisen and Savenije (2015), and Zhang and Savenije (2017), together with the present experiments. The thick red line represents the $\gamma = \chi$ boundary, whereas the thick blue solid line the $\gamma = \chi^{1/3}$ law.

However, as noted by Toffolon et al. (2006), the selected parameters in the cited studies mixed different variables that depend on the evolution of the process itself, whereas Toffolon et al. (2006) defined the governing parameters of the process based on external quantities. Note that as *external* they intended quantities simply based on the geometry of the domain and on the main characteristics of the tidal forcing. Therefore, we decided to follow the approach by Toffolon et al. (2006) using their convergence ratio parameter (γ), that is related to the planimetric scales of the estuary, and the friction parameter (χ), defined as the ratio between friction and inertia. These two dimensionless parameters are written as:

$$\gamma = \frac{L_g}{2\pi L_b}, \qquad \chi = \epsilon \frac{L_g}{2\pi C^2 R_h}, \qquad \text{with} \qquad L_g = T\sqrt{gR_h}, \tag{9}$$

where $\epsilon = a/R_h$ is the nondimensional tidal amplitude, R_h is the mean hydraulic radius of the channel, L_b is the convergence length, and L_g is the length of an inviscid small amplitude tidal wave propagating on constant flow depth R_h. Differently from the original definition, we substituted the hydraulic radius to the mean flow depth, as it is more appropriate in the case of complex cross-sections with tidal flats.

Based on the above choice, we decided to design the present experiments preserving the friction to inertia ratio χ and the form factor F and, finally, to impose a scale distortion along the three spatial coordinates. Scaling arguments will be resumed in Section 6.2, where we describe the dispersion regime with the aim to extend the laboratory measurements to the estuaries scales. However, the introduction of multiple constituents as analytically represented by Equation 2 is characterized by the presence of two different tidal periods, thus raising problems when one typical time scale must be selected for the evaluation of the external parameters of Equation 9. Note that Toffolon et al. (2006) and later Cai et al. (2012) applied their models to realistic estuaries where tides are characterized by lunar and solar constituents with different periods, but dominated by the semi-diurnal lunar tide M_2. In the present study, we defined the nondimensional tidal amplitude as the ratio between half of the tidal range, defined as the difference between the highest and lowest water level, and the hydraulic radius. We recall that all the three series of experiments with multiple components were designed in order to maintain the same tidal range, while varying the form factor and the phase shift. As far as the typical tidal period is concerned, we select the dominant period associated with of the higher amplitude constituent. Thus, the friction parameter χ was calculated accordingly.

Since we imposed a similitude based on the parameter χ, we are now interested to understand what kind of estuaries our experiments refer to, according to the classification reported in Toffolon et al. (2006). Figure 2 shows the values of the parameters χ and γ of several real estuaries (Cai et al., 2012; Gisen & Savenije, 2015; Lanzoni & Seminara, 1998; Toffolon et al., 2006; Zhang & Savenije, 2017) together with those associated to the present experiments. Depending on the values of γ and χ, estuaries fall in one of the four different parameter regions, being namely weakly/strongly dissipative and weakly/strongly convergent. The red solid line indicates the case $\gamma = \chi$ meaning that gravity and inertia have exactly the same weight and the blue solid line represents the condition $\gamma = \chi^{1/3}$ whereby the gravitational effects balance the frictional ones (Toffolon et al., 2006). Our experiments (blue triangles and purple diamonds) fall in the weakly dissipative and weakly convergent region close to the boundary $\gamma = 1$, that corresponds to the balance between friction and inertia. Thus, the measurements presented in the rest of the paper can be considered representative of the behavior of real weakly dissipative estuaries with an almost constant channel width. Finally, note that in our physical model, the channel has lateral tidal flats that might play an important role in the hydrodynamic and dispersion processes.

It is worth mentioning that the tidal waves reproduced in our experiments are all far from the resonance conditions, defined as $L_g/L_{ch} = 4$, where L_{ch} is the length of the tidal channel except for the case with $T = 100$ s, that is, $L_g/L_{ch} = 4.4$, where the hydrodynamic conditions are close to resonance. The amplification of the tidal waves

along the channel has been monitored with level gauges and few examples are reported in the Supporting Information S1 (Figure 1).

Finally, we acknowledge the limitation of the present experimental setup regarding the simplified geometry, which cannot represent entirely the complexity of a natural system (estuary, tidal bays, or small lagoons). However, our laboratory flume and the designed geometry (tidal inlet and nonuniform compound tidal channel) represent an improvement with respect of previous studies (Nicolau del Roure et al., 2009; Vouriot et al., 2019; Wells & van Heijst, 2004). Moreover, we are aware that in several context the presence of a river discharge is also a fundamental driver of the circulations. However, in the present context we intended to focus only on the role of the periodic flows generated by a tidal wave, leaving for future analysis the inclusion of a river input.

5. Eulerian Analysis: Time-Dependent Flow and the Generation of a Residual Current

The periodic character of the forcing tide induces an unsteady flow field, which in general is 3D and whose intensity depends on tide propagation within the estuary.

Here we collect 2D free surface velocity fields which are a good approximation of the real flow fields, since shallow water approximation is usually assumed valid owing to the strong scale separation between the vertical and planimetric dimensions. In the present experiments, the ratio λ_L between the typical vertical length scale (water depth) and the typical horizontal length scale, over we assist to main velocity variations, is about 10^{-2}. The shallow water approximation implies that the momentum balance along the vertical direction leads to an hydrostatic pressure distribution, and the vertical velocity component and its gradients are negligible with respect to the horizontal components. To assume valid this assumption, two conditions should hold. First, the nondimensional group $F_r^2\lambda_L^2$ should be much less than 1. Note that F_r is a typical Froude number defined as $F_r = U/\sqrt{gR_h}$ with U being the typical horizontal velocity scale. This condition guarantees that the convective terms in the vertical momentum equation are negligible with respect to the gravitational term. Second, the nondimensional group $F_r^2\lambda_L/C$ should be much less than 10, which implies that the gravitational term is much greater than the divergence of the Reynolds stresses. In the present experiments both groups are of the order of about 10^{-5}. Thus, we can safely assume that the flow develops in shallow water conditions. Residual 3D effects linked to the compound cross-section geometry, which generate secondary flows, are known to act on very limited regions close to the bottom corners (Shiono & Knight, 1991; Stocchino et al., 2011).

Moreover, the presence of an inlet always induces the generation of large-scale shallow vortices owing to the emission of vorticity at its corners and the consequent development of shear layers (Nicolau del Roure et al., 2009; Vouriot et al., 2019). These macro-vortices are recognized to be 2D structures being much wider than deep (Jirka, 2001) able to control the momentum, mass, and sediment exchanges between the estuary and the outer sea (Blondeaux & Vittori, 2020; Wells & van Heijst, 2004). Dispersion is also influenced by another process typical of periodic flows in estuaries that plays a fundamental role over time scales of many tidal cycles, the so called residual current that can be revealed applying a temporal decomposition based on the tidal period (Jay, 1991; Valle-Levinson, 2010).

In this section we first discuss the 2D free surface unsteady flow and the consequent generation of inlet macro-vortices and, second, the characteristics of the 2D free surface residual currents.

5.1. Time-Dependent Velocity Fields and the Dynamics of Inlet Macro-Vortices

Figure 3 reports examples of the 2D velocity fields with contours of the Okubo-Weiss parameter λ_0 for the experiment 26-SC and experiment 05-MC as typical examples of the single and multiple components tides respectively. Note that, Okubo-Weiss parameter λ_0 is a commonly used parameter for classifying flow patterns and in particular to identify vortices (Okubo, 1970; Weiss, 1991).

Panels (1) and (2) report the time evolution of the longitudinal velocity at the inlet mouth and the markers represent the time where the snapshots of the 2D velocity fields were taken during flood and ebb phases. In particular, panels (a1)–(d1) show four snapshots taken during the flood phase, whereas panels (a2)–(d2) refer to the ebb phase. To help the identification of the main flow structures, we focused on the area around the inlet, located around $x = 4$ m. Note that the geometry of the inlet used in the present study is identical to the *barrier*

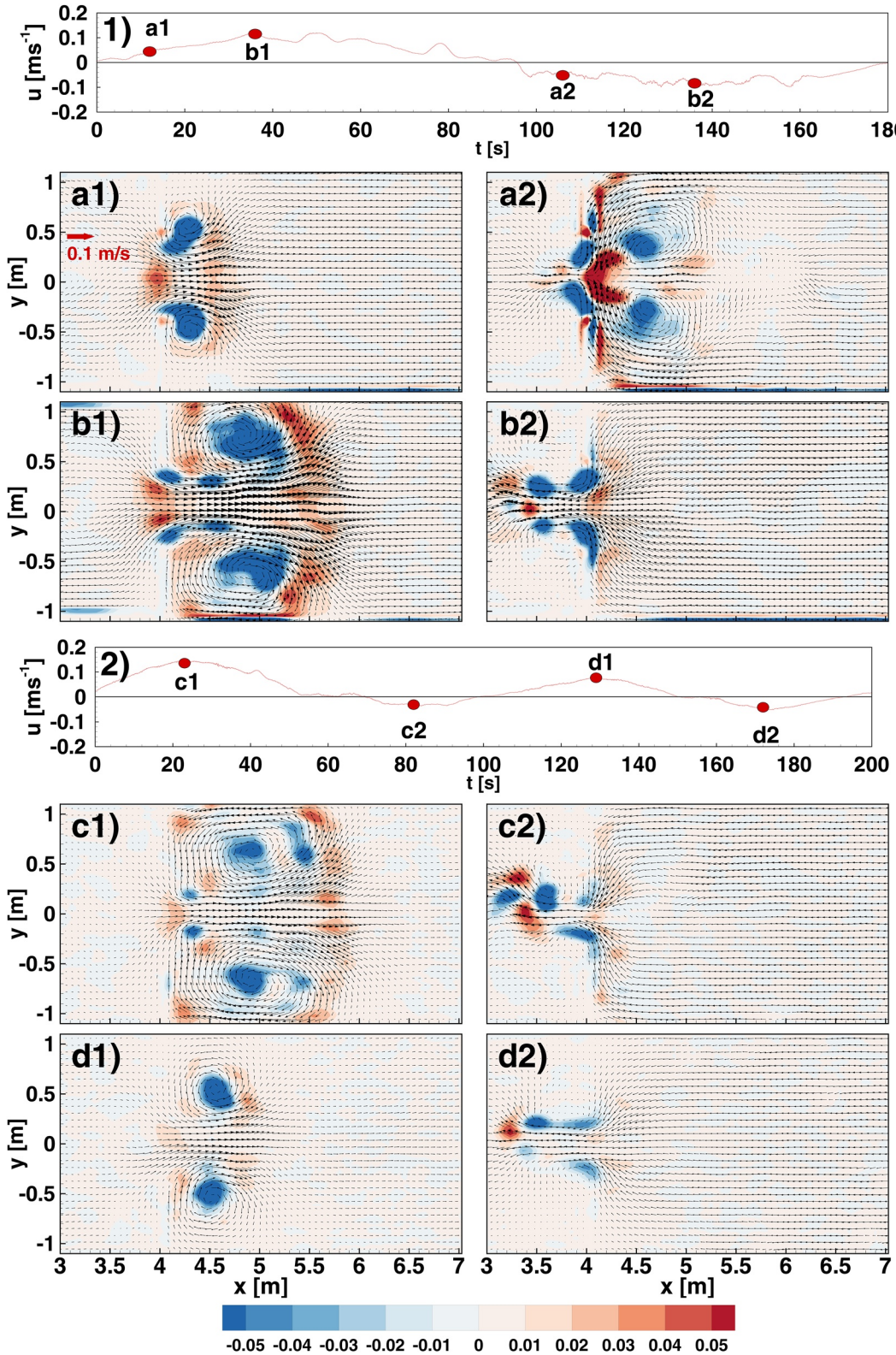

Figure 3. Panels (1) and (2): time signal of the longitudinal velocity measured at the inlet mouth for experiments 26-SC and 5-MC with the markers indicating the time instant of the 2D maps. Free surface velocity fields at different times with the contours of the Okubo-Weiss parameter λ_0 superimposed. Experiment 26-SC: Panels (a1) and (b1) during the flood phase and panels (a2) and (b2) during the ebb phase in single series. Experiment 05-MC: panels (c1) and (d1) during the flood phase and panels (c2) and (d2) during the ebb phase. Note that the domain reported is restricted to the region around the inlet.

island analyzed in Nicolau del Roure et al. (2009). In their study, however, the authors tested also different other configurations of the inlets in a shallow basin, without tidal flats, with the aim to understand the trajectory of the vortex cores during a tidal cycles.

As in the cited study, the generation of the macro-vortices during the flood phase is found to be controlled by the inlet corners that act as a source of vorticity that is then convected towards the tidal channel. From the time sequence shown in Figure 3 during the flood phase (panels (a1) and (b1)), it is clearly visible that small-scales vortices are emitted with a period much shorter than the tidal one and, more interestingly, that they tend to merge forming the larger structures that occupy the entire tidal flats width (panel (b1)), leaving a strong jet in the center-line of the channel (red regions for $\lambda_0 > 0$). The mechanism of vortex merging is shown in detail in the movies provided as supplementary material for both single and multiple tidal components. From the time series of velocity fields (shown in the movies), it is possible to estimate the vortex shedding frequency, which assumes a value of about 0.3 s^{-1} and a corresponding Strouhal number of about 0.2, in accordance with known results on vortex shedding generated by bodies or structures (Davis & Moore, 1982; Sumer, 2006).

Comparing the single component experiments and the multiple components cases, the generation and evolution of the flood-macrovortices are further complicated by a multiple-constituents forcing with different shapes and phase lags of the two harmonics. For very low and high values of the form parameter F, the tides are mainly semi-diurnal and diurnal, respectively, that is, dominated by a single harmonic. In these cases, the flood-macrovortices show the same behavior observed in the single harmonic experiments. More interestingly, in the cases of mixed tides, that is, for $0.25 < F < 3$, the tidal oscillations show more than one crests and troughs within a tidal cycle. Two different classes of flood-macrovortices are thus generated depending on the tidal wave crests. In fact, a larger size macrovortices is formed in the flood phase corresponding to the maximum crest, see panel (c1). The size of the latter structure is comparable to the macrovortices generated in the case of the single harmonic forcing with the same period and relative amplitude. The flood-macrovortices are then flushed away during the ebb phase, see panel (c2). Secondary macrovortices, the size of which is significantly smaller (see panel (d1)) are generated in correspondence of the second, less intense, tidal crest. Also these second macrovortices are flushed away during the ebb phase (panel (d2)).

The mechanisms leading to the observed macro-vortices generation were already pointed out by Nicolau del Roure et al. (2009), who described it as the entrainment of small-scale vortices in the main vortical structure. When a compound geometry is considered, the depth gradient between the tidal flats and the main channel is a further source of vorticity generation. This feature was investigated by Brocchini and Colombini (2004), who derived the vorticity and enstrophy equations for shallow flows giving rise to new terms proportional to the span-wide depth jump. This mechanism is fundamental for the generation of macro-vortices in turbulent uniform flows (Stocchino et al., 2011; Stocchino & Brocchini, 2010) and, also in case of periodic forcing as in our experiments, it could sustain the vorticity generated at the inlet and along the main channel. However, in the periodic flow case, differently from the uniform channel flow conditions, these vortices are transient structures depending on the intensity of the flood/ebb flow within the channel and far from the inlet. It is worth noting that in our experiments the values of depth ratio parameter $r_h = y_{mc}/y_{tf}$, defined as the ratio between the water depth in the main channel y_{mc} and the water depth in the tidal flat y_{tf} (Stocchino et al., 2011), vary according to the free surface variations in a tidal cycle, but are always larger than 3. This suggests that namely all experiments are in *shallow water* conditions following the classification of flow regimes in compound channels suggested by Nezu et al. (1999) and commonly adopted (Enrile, Besio, & Stocchino, 2018; Shiono & Knight, 1991; Van Prooijen et al., 2005).

As far as the typical dimensions of the inlet macro-vortices are concerned, they are bounded on the span-wise direction between the main channel and the side walls, whereas their stream-wise extension depends on the intensity of the mean flow and, ultimately, on the friction parameter χ. In fact, the vortices are found to be strongly elongated in the longitudinal direction and to scale from 1 to $5l_i$ (see Figure 1, for notation).

During the ebb phase, see Figure 3 panels (a2)–(d2), an intense outward jet is formed and penetrates into the basin for few meters. The jet is highly turbulent and small-scale vortices are generated and transported with the jet. Moreover, for the range of parameters investigated, the flood macro-vortices are always flushed away during ebb. The condition by which the flood-vortices are flushed or trapped in the channel within a tidal period is usually described in terms of Strouhal numbers, defined as $S_t = L/UT$, where L is a typical length scale related to the vortex shedding generation, U is a convective velocity scale, and T is the tidal period. The importance of the

role of the Strouhal number or its inverse, namely the Keulegan-Carpenter parameter, in the dynamics of the tidal macro-vortices or vortices generated by headlands has been recognized by several authors (Davies et al., 1995; Nicolau del Roure et al., 2009; Signell & Geyer, 1991; Vouriot et al., 2019; Wells & van Heijst, 2004).

In context similar to the present one, Wells and van Heijst (2004) defined three classes of vortices depending on S_t, built with the inlet width and the tidal peak velocity. In particular a critical value, $S_{tc} = 0.13$, discriminates between vortices that are completely flushed away in a tidal cycle ($S_t < S_{tc}$) and vortices that do not completely decay within a cycle ($S_t > S_{tc}$). In the present case, we obtain values of S_t that exceed 0.13 only for the lowest tidal amplitude (exp. 8-SC, 13-SC, 18-SC, and 23-SC). However, even in those cases the flood-vortices are flushed away in the ebb phase, contrary to the observation of Wells and van Heijst (2004), Nicolau del Roure et al. (2009), and Vouriot et al. (2019).

A possible explanation could be found in the compound geometry that enhances ebb velocities. The presence of tidal flats were thus indicated as a source of ebb dominance (Kang & Jun 2003). Different parameters can be used to evaluate the ebb/flood asymmetry in tidal flows, for example, ebb time (Kang & Jun 2003). In the present study, we employed the tidal power per unit mass P defined as the time integral of the kinetic energy per unit mass. We thus calculated the tidal powers associated to the flood and ebb phases separately and then estimated their ratio $\Pi = P_{ebb}/P_{flood}$ which indicates ebb or flood dominance whether it assumes values greater or lower than unity. Within the experimental errors in computing the power ratio, all experiments, with only one exception (however characterized by value of Π very close to unity), are ebb dominated, thus, confirming previous observations (Aubrey & Speer, 1985; Friedrichs & Madsen, 1992; Geng et al., 2020). See Supporting Information S1 for the details of the computation and the results.

5.2. Shape and Intensity of the Residual Current

In the previous section, we described the time-dependent 2D velocity fields generated by the monochromatic and multiple harmonics tidal oscillations and the consequent generation of large-scale vortical structures. We also commented on the transient nature of the above macro-structure. Indeed, the flood-vortices grow and disappear in a single tidal cycle. However, it is well known that the periodic oscillations due to tides not only generate a time-dependent flow, but also a steady current known as residual current. As far as any kind of mass transport (sediment, nutrients and biogeochemicals) is concerned, it becomes relevant after several tidal cycles and this is mainly due to the appearance of the residual currents, often referred to as "tidal pumping" that may lead to significant longitudinal dispersion (Banas et al., 2004; Jay, 1991; Valle-Levinson, 2010; Zimmerman, 1986).

The free surface residual current can be obtained by averaging the time-dependent free surface velocity fields over a tidal period, decomposing the velocity fields as: $\mathbf{u}(\mathbf{x}, t) = \mathbf{u}'(\mathbf{x}, t) + \mathbf{U}(\mathbf{x})$, where $\mathbf{U}(\mathbf{x})$ represents the Eulerian free surface residual current, no longer time dependent (Jay, 1991), and the $\mathbf{u}'(\mathbf{x}, t)$ is still a time-dependent velocity field that could be, in principle, further averaged over a typical Eulerian integral scale to filter out the turbulent fluctuations (Valle-Levinson, 2010).

Figures 4a–4e report examples of the velocity vectors with superimposed contour plot for the magnitude ($|\mathbf{U}(\mathbf{x})|$) of the 2D free surface residual current for experiments characterized by a single component tidal forcing with the same tidal period and different tidal amplitudes, panels (a) to (c), and, for experiments characterized by multiple components tide, with two different values of the form factor F, panels (d) and (e). As a general comment, we observe that the resulting Eulerian residual current is perfectly symmetrical with respect to the main channel, as expected in a symmetrical domain. The flow pattern is quite regular away from the inlet mouth and mainly governed by the presence of two macro-vortices on the tidal flats and of smaller vortical structures on the basin side.

The normalized tidal amplitude ϵ increases from panel (a) to panel (c) influencing both intensity and shape of the residual current. Indeed, intensity and dimension of the tidal flats macro-vortices increase as ϵ increases. Variations of the tidal period are less relevant in this case as the generation of the residual current is mainly due to the tidal amplitude (maps of the residual current at different periods are provided as additional material in Supporting Information S1). Moreover, it clearly appears that the shape of the residual currents does not substantially change with F, see panels (d) and (e). The shape of the fields of $\mathbf{U}(\mathbf{x})$ is strongly related to the macrostructures presented in the previous section. It seems that the transient flood-vortices averaged over a tidal cycle leave their

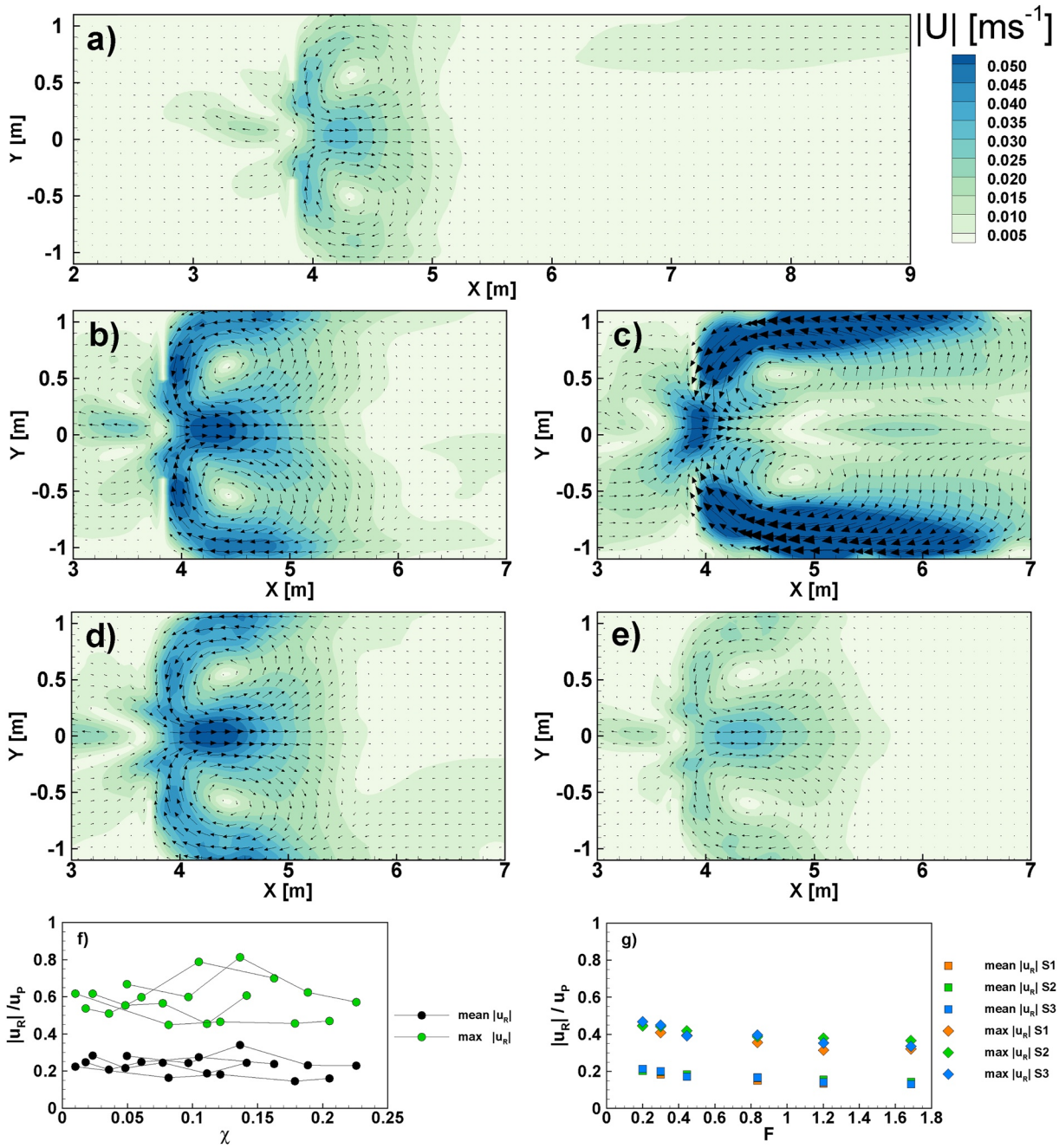

Figure 4. Panels (a) to (c): examples of free surface residual current fields for the experiments 13-SC, 14-SC, and 17-SC. Panels (d) and (e): examples of free surface residual current fields for the experiments 2-MC and 7-MC. Panel (f): ratio of mean and max residual current velocity compared to the peak tidal velocity as a function of the parameter χ. Panel (g): ratio of mean and max residual current velocity compared to the peak tidal velocity as a function of the parameter F.

signature in the generation of the residual current. The stream-wise extension of the vortical structures shown in Figures 4a–4e is identical to the maximum size of the flood-vortices during the flood phase.

In Figures 4f and 4g, we reported the ratios of both the peak and mean velocity of the residual current, defined as the mean of the 10% of the maximum measured values, normalized with the peak tidal velocity measured at the inlet as a function of the friction parameter χ for the single-component experiments, and of the form factor F for the multiple harmonics cases. Depending on the controlling parameters, the intensity of the residual current could reach values up to the 80% of the maximum velocity registered in the unsteady field. However, in the range of parameters investigated, the maximum and mean $|U_R|/U_p$ remains fairly constant.

We are taking the measurements of the free surface velocities and this is somehow acceptable since the flow can be regarded as mainly 2D. However, the time-dependent flow and, thus, also the residual current is a 3D field. Regarding the residual current this implies that mass conservation is satisfied assuming that at both ends of the flume the flow is 3D and that, at the bottom, the flow is reversed compared to the free surface layer.

Finally, we expect that the measured residual current strongly impacts on the Lagrangian mass transport and, ultimately, on the dispersion regimes. Zimmerman (1986) already noted the importance of the residual currents on the mass transport and that, in some cases, the complexity of the flow patterns may lead to chaotic mixing (Beerens et al., 1994; Ridderinkhof & Zimmerman, 1992) and the appearance of complex fluid deformation patterns that nowadays are recognized as Lagrangian coherent structures (Orre et al., 2006). In the Supporting Information S1 we reported the residual current fields for all experiments.

6. Lagrangian Analysis and Dispersion Regimes

One of the main goals of the present study is to assess the dispersion processes occurring in weakly dissipative tide-dominated estuaries characterized by the presence of an inlet mouth and a tidal channel with lateral flats. In the rest of this section, we will present the main results obtained from the experimental measurements in terms of single and multiple-particles statistics as presented in Section 5.

6.1. Lagrangian Integral Scales

We start our analysis showing the computed autocorrelation functions and the corresponding Lagrangian integral time scales. The shapes of the correlation function and their integral, namely the Lagrangian Integral Scale, are strongly related to the expected dispersion regimes (Taylor, 1921).

Figure 5 shows the autocorrelation functions $\mathcal{R}_{uu}$ (panels (a) and (b)) for several single and multiple-component experiments and $\mathcal{R}_{vv}$ (panels (c) and (d)) for the same multi-component experiments of panel (b) as functions of time, along with the corresponding Lagrangian time scale T_L normalized with the tidal period T as a function of the parameter χ (panel (e)) and of the parameter F (panel (f)), depending on the series considered.

In all cases, the flow is mainly unidirectional as shown by the rapidly decaying of the spanwise autocorrelation $\mathcal{R}_{vv}$; thus, providing a small contribution to the overall value of T_L. The streamwise autocorrelation functions show a strong looping-like shape in all the cases. The intensity of the negative and positive lobes is inversely dependent on the relative tidal amplitude ϵ (panel (a)). This is consistent with the fact that the periodic flow intensifies as the amplitude increases, leading to a decrease in the $\mathcal{R}_{uu}$. Tidal period variations for a fixed amplitude produce smaller difference in the streamwise autocorrelation structure. Moreover, following Enrile et al. (2019), we investigated the possible influence of the initial conditions associated to particle release. To this end, in the multiple component series, we performed a sequence of Lagrangian computations, releasing the numerical particles at different times during a single wave period and we computed our target functions ($\mathcal{R}_{uu}$, $\mathcal{R}_{vv}$, and the corresponding integral scales) averaging them. The low variability of the computed autocorrelation functions is shown as grey shaded area in panels (b)–(d). For the single harmonic experiments there is no effects of the different releasing time. The independence from the initial releases of the numerical particles will be re-discussed in terms of absolute dispersion in the next section.

The integral time scales show monotonic decrease as the friction parameter increases, see panel (e). The values of T_L are found to be in a range between 0.03 and 0.28T for the investigated values of χ. Interestingly, it seems that the Lagrangian integral scale attains an almost constant value for $\chi > 0.15$. Panel (e) reports also a power fitting of the nondimensional Lagrangian integral scale as a function of the friction parameter χ, which shows that the fitted trend can be written as:

$$\frac{T_L}{T} = 0.0025\chi^{-0.98} + 0.037 \tag{10}$$

with a goodness of fit $R^2 = 0.82$.

The predicted asymptotic value is then 0.037 for increasing χ, suggesting that for dissipative estuaries/tidal embankments the Lagrangian time could be regarded as constant and equal to the portion of the dominating tidal

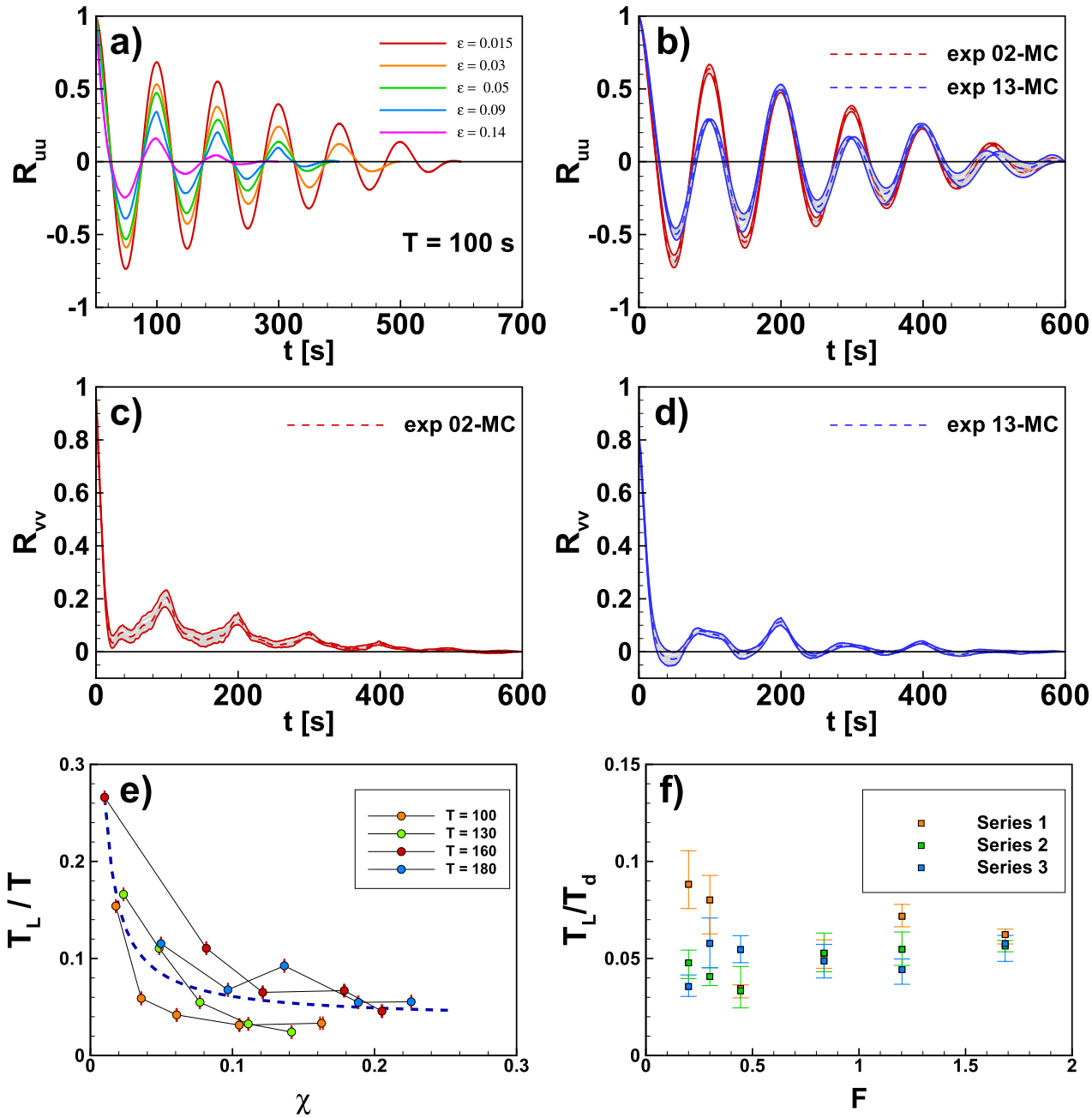

Figure 5. Lagrangian autocorrelation functions and integral time scales as a function of the tidal amplitude, period, and parameters χ and F. (a) Longitudinal autocorrelation function $\mathcal{R}_{uu}$ for varying nondimensional tidal amplitude ϵ for a fixed value of the tidal period $T = 100$ s of single component series. (b) $\mathcal{R}_{uu}$ for experiments 2-MC and 13-MC. (c) $\mathcal{R}_{vv}$ experiment 2-MC. (d) R_{vv} experiment 13-MC. (e and g) Nondimensional Lagrangian integral time scale T_L/T as a function of the parameter χ and form factor F, respectively.

period. This result is also used in the next section where the dispersion coefficients are discussed. Moreover, T_L remains always much shorter than the tidal period also for multiple harmonics tides (Figure 5f) and, consistently with the trend found in χ, it maintains fairly constant values as the form factor and the phase shift ϕ vary.

The fact that T_L is always smaller than the tidal period T implies that a diffusive regime is likely to occur after a much shorter time compared to the external time scale (T). Moreover a diffusivity coefficient can be defined since a region in which the absolute dispersion depends linearly on time can be recognized. This also means that the tidal period is a good choice as a reference external scale for estuary classification (Toffolon et al., 2006)

but less significant to discriminate among the different dispersion regimes. A decorrelation time smaller than the tidal period has also been found in dispersion analysis based on field data (Enrile et al., 2019). However, the periodicity imposed by the tidal forcing could be responsible for the looping-like behavior of $\mathcal{R}_{uu}$ and, as we will see in the next section, it might also affect the long time behavior of the total absolute dispersion $a^2(t)$. Note that looping autocorrelation could be triggered also by the presence of large-scale vortical structures as noted in Berloff et al. (2002) and Veneziani et al. (2004).

6.2. Single Particle Statistics and Dispersion Coefficients

Longitudinal dispersion is known to be produced or influenced by several mechanisms such as shear dispersion owing to periodical flows, macro-vortices, and a steady residual current. We investigated how the interaction between a periodic tidal forcing, an inlet mouth, and a compound channel triggers a fairly complex flow where all the latter mechanisms are active. Maps of the Okubo-Weiss parameter showed the presence of both elliptical (vortices at different scales) and hyperbolic regions (intense shear structures) in the domain with a markedly nonstationary character. We performed the single particle statistics analysis, see Equation 4, starting from two different Eulerian velocity fields, namely the complete unsteady field ($\mathbf{u}(\mathbf{x}, t)$) and the associated residual current ($\mathbf{U}(\mathbf{x})$). The reason will be clear when we will discuss the time behavior of $a^2(t)$. A second important preliminary comment refers to the kind of dispersion coefficients (K) we estimate. As noted by Besio et al. (2012) the output of the single particle statistics analysis might produce coefficients that are related to several mixing processes and this depends on the starting Eulerian field assumed to compute the trajectories of numerical particles. In the present case, the only flow decomposition that we performed is an average over the tidal period in order to generate the residual fields and no other averages have been performed (e.g., a moving average of the unsteady fields to isolate turbulent fluctuations). This means that our procedure yields to the estimate of a longitudinal coefficient (K_x), a transverse coefficient (K_y), and a total diffusive coefficient ($K = K_x + K_y$) that include also the turbulent diffusion contribution. All the dispersion properties will be presented in nondimensional form using as scaling quantity the ensemble averaged Lagrangian kinetic energy per unit mass $E_L = 1/2\langle(u_L(\mathbf{x},t)^2 + v_L(\mathbf{x},t)^2)\rangle$ and the Lagrangian integral scale T_L, where the brackets $\langle\bullet\rangle$ indicate an ensemble average over the particles released.

The results presented in the following are derived from numerical integration of particles uniformly released over the entire tidal channel. The particles were released on a regular grid with a spacing equal to half of the PIV mesh of the Eulerian measurements. Tests with a different number of particles were performed increasing the spacing four times: the computed statistics did not change. In the case of multiple-component tides, the absolute dispersion was evaluated using several initial deployment times, as for the autocorrelation functions.

Note that a uniform seeding is the standard procedure when single (and multiple) particle statistics is studied (LaCasce, 2008). A drawback of the latter is the assumption of homogeneous flow conditions, which most of the time is not valid for geophysical applications. Flow inhomogeneities are present also in the flow at hand, that is, the region around the tidal inlet is strongly affected by large-scale macro-vortices, whereas the channel far from the inlet is more uniform. However, we consider useful the implementation of this approach in order to characterize the behavior of the tidal mixing generated by the presence of an inlet also based on the common approach to study water quality using numerical models of the advection-diffusion equation (e.g., water quality module of Delft3D, Mike21, FVCOM) that requires the definition of global dispersion coefficients, see Ren et al. (2014), Alosairi and Alsulaiman (2019) among many others.

Figure 6 summarizes results of the single particle statistics for the entire set of experiments for both single and multiple component tides. Panel (a) displays the typical behavior of the time dependence of the nondimensional absolute dispersion $a^2(t)/\left(E_L T_L^2\right)$ for the unsteady velocity case (solid lines) and for the residual current case (dash-dotted lines) against the nondimensional time t/T_L in three experiments of the single harmonic tide taken as examples (exp. 14-SC, 15-SC, and 16-SC). Considering the results for the absolute dispersion computed with the time-dependent Eulerian fields, different regimes are visible depending on the time.

For time lower than T_L a ballistic regime is observed and, then, for $\mathcal{O}(t/T_L) \sim 1$ a super diffusive regime appears and lasts for few integral time scales. Super diffusive regimes are usually related to intense negative lobes in the auto-correlation functions (Berloff et al., 2002; Veneziani et al., 2004), as also observed in the present experiments. High anticorrelation is observed in all experiments, see Figures 5a and 5b, after the first zero of $\mathcal{R}_{uu}$ regardless the controlling parameters and this yields to a regime where $a^2(t)/\left(E_L T_L^2\right) \propto (t/T_L)^\alpha$ with $\alpha \simeq 2 \div 3$.

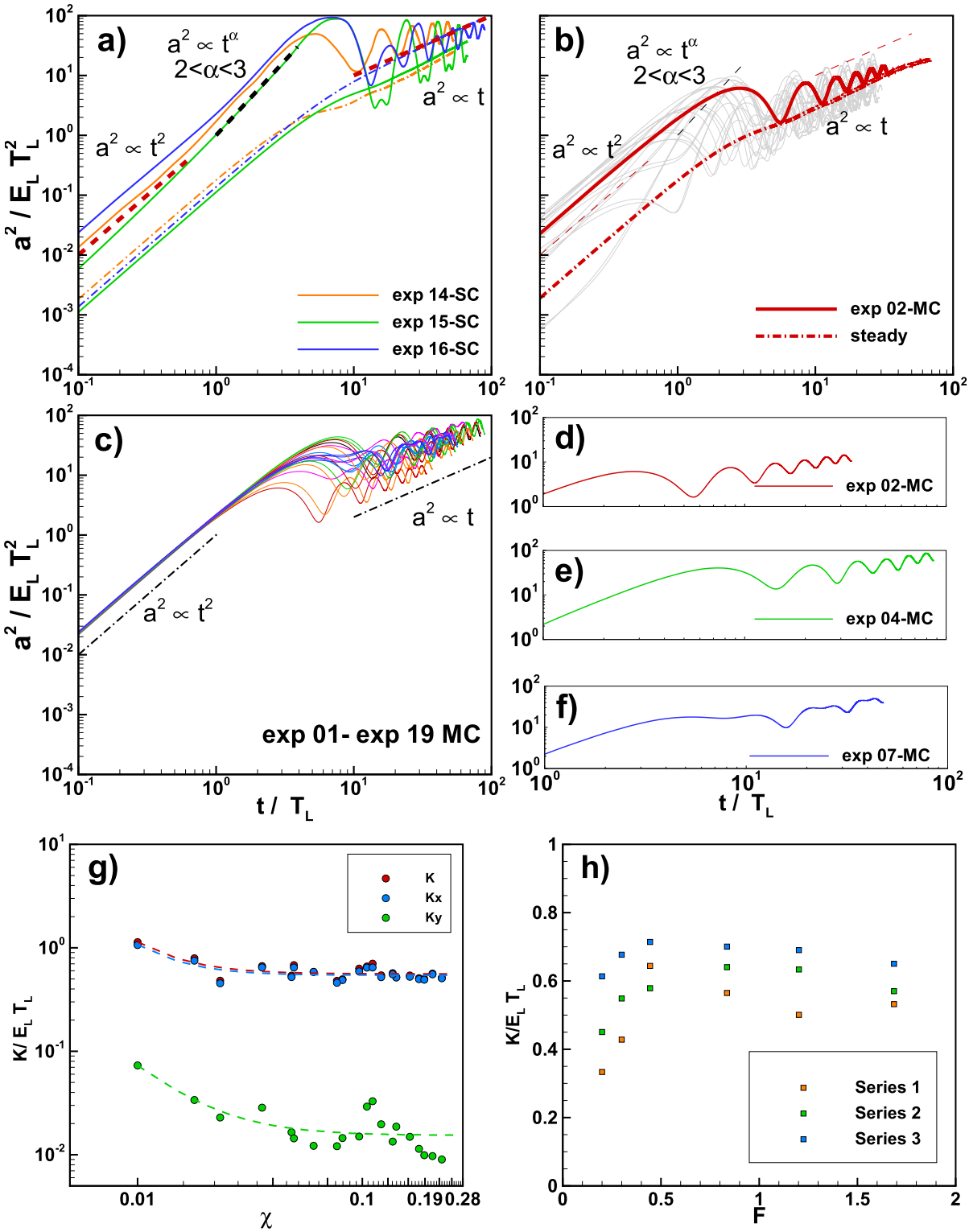

Figure 6.

For longer times, $t/T_L > 10$, the nondimensional absolute dispersion shows an oscillating behavior with a periodicity proportional to the tidal period. Interestingly, the oscillations hide a linear growth in time that is revealed by the absolute dispersion computed using the residual current only (dash-dotted lines). Indeed, for each experiment, $a^2(t)/\left(E_L T_L^2\right)$ computed using the field $\mathbf{U}(\mathbf{x})$ seems to smooth out the super diffusive regime and the oscillations for longer times, displaying the standard picture of a ballistic regime for time lower than few T_L and a diffusive (linear regime) for longer times.

Panel (b) shows the results of a typical experiment when the tidal signal is composed by two harmonics, namely experiment 2-MC. Grey lines represent the output of single deployment, whereas the solid red line the average over the different releases of the total absolute dispersion. The effects of the initial conditions are clearly visible and produce a bundle of curves that, however, tend to similar regimes for long times. This has been also observed by Enrile et al. (2019) where the spread of the different curves was calculated and a decrease in time was observed. Physically, this suggests that after several tidal cycles the particles are no longer influenced by their initial conditions. However, this further time scale of the process must not be confused with the Lagrangian integral scale T_L that separates the *ballistic* regime from the *Brownian* regime, when the latter exists. As discussed in Enrile et al. (2019), this time scale longer than the integral scale should be interpreted as a quantity that measures how strong is the effect of the initial conditions (e.g., release time within the tidal cycle) with respect to an average value attained for longer times. Interestingly, all total absolute dispersion curves tend to a diffusive regime for $t/T_L \gtrsim 10$ regardless the initial conditions, which is well described by the averaged $a^2(t)/\left(E_L T_L^2\right)$ (red solid line).

Even in this case, for $t/T_L \lesssim 1$, a *ballistic* regime is always recovered, whereas super-diffusive regime $a^2(t)/\left(E_L T_L^2\right) \propto t^{2\div3}$ appears only for some particle deployments and this is coherent with the autocorrelation functions that might show intense positive lobes after negative ones, see Figure 5. Moreover, panel (b) also reports the nondimensional total dispersion evaluated using the residual currents only (dash-dotted lines). As for the single harmonic experiments, the residual currents lead to a time dependence of the total absolute dispersion that substantially filters out the oscillations due to the periodic velocity fields, leaving unaltered the overall slope of the curves. This could demonstrate how the net particle dispersion is produced by the residual currents as claimed in tidal flows (MacCready, 1999; Valle-Levinson, 2010).

The total nondimensional averaged dispersion for all multiple component experiments is plotted in Figure 6c. Averaging over a great number of initial conditions leads to hidden possible super-diffusive regimes and all curves to collapse onto a *ballistic* initial regime. All experiments shown in panel (c) reach an asymptotic diffusive regime with some behaviors related to the shape of the tidal waves. In particular, the oscillations observed for $t/T_L \gtrsim 10$ depend on the form factor F and show typical periods depending on its values, see panels (d)–(f) where three experiments are displayed. Experiments 2-MC and 4-MC are characterized by tidal waves dominated by the semi-diurnal components, $F = 0.2$ and $F = 0.4$, respectively, whereas experiment 7-MC corresponds to a mainly diurnal mixed tide ($F = 1.6$). The observed oscillations are coherent with the dominant frequency of the forcing tides.

The dispersion coefficients (K, K_x, K_y) were calculated performing a linear regression of the nondimensional absolute dispersion for times $t/T_L \gtrsim 10$. The obtained values, scaled by $E_L T_L$, are plotted in Figure 6 as a function of the external parameter χ for the single harmonic cases, panel (g), and as a function of the form factor for the multiple components experiments, panel (h). Not surprisingly the greater contribution is given by the longitudinal coefficient K_x that turns out to be two orders of magnitudes greater than the spanwise coefficient K_y, see panel (g). This is true also for the multiple components experiments.

The dimensionless dispersion coefficients can be again fitted with a power law as a function of χ in the case of single component tides, as done for the Lagrangian integral scale. The fitting laws read:

$$\frac{K}{E_L T_L} = 1.7 \times 10^{-5} \chi^{-2.26} + 0.560 \tag{11}$$

Figure 6. Panel (a): Examples of the nondimensional absolute dispersion $a^2(t)/\left(E_L T_L^2\right)$ as a function of nondimensional time t/T_L for experiments 14-SC, 15-SC, and 16-SC; dotted lines indicate the time laws for the dispersion regimes and dash-dotted lines the absolute dispersion derived from the residual current fields. Panel (b): Nondimensional total absolute dispersion as a function of the nondimensional time for experiment 2-MC; grey lines refer to different initial particles releasing, red solid lines to their averaged, and red dash-dotted lines indicate the total absolute dispersion inferred from the residual current flow. Regimes are plotted in dashed lines. Panel (c): Averaged total absolute dispersion for all experiments. Focus on linear regimes in multiple component series: (d) experiment 2-MC, (e) experiment 4-MC, and (f) experiment 7-MC. Panel (g) and (h): Nondimensional horizontal dispersion coefficients (K, K_x, K_y)/($E_k T_L$) as a function of the parameter χ and F, respectively. Dotted lines in panel (g) represent the fitting laws reported.

$$\frac{K_x}{E_L T_L} = 9.4 \times 10^{-6} \chi^{-2.37} + 0.540 \quad (12)$$

$$\frac{K_y}{E_L T_L} = 7.5 \times 10^{-6} \chi^{-1.94} + 0.015 \quad (13)$$

with goodness of fit R^2 equal to 0.75, 0.75, and 0.81, respectively. Two aspects are worthy to be noted. First, the choice of χ as a controlling external parameter is suitable not only for the hydrodynamic characterization (Cai et al., 2012; Toffolon et al., 2006) but also to globally describe the asymptotic dispersion regimes. Second, the results suggest that for increasing friction parameter the nondimensional coefficients tend to become constant and this is consistent also with results obtained in river dispersion, whereas for increasing friction the dispersion coefficients tend to be independent from the friction parameters itself (Besio et al., 2012; Chau, 2000; Webel & Schatzmann, 1984). In the present case, for increasing χ, $K/(E_L T_L)$ and its main contribution $K_x/(E_L T_L)$ tend to a value around 0.5, which is slightly higher than the measurements reported in the cited works that predicted a value around 0.3. The increased asymptotic values could be explained by a stronger nonuniformity of the flows at hand compared to a uniform, unidirectional river flow.

In classical Taylor's theory (Taylor, 1921), the turbulent diffusion coefficient is connected to a typical time scales (the Lagrangian integral scale) and to a typical velocity scale squared, as long as the diffusive regime is recovered. In fact, the dispersion coefficient can be defined as: $K = \rho_L^2 T_L$, where the velocity variance ρ_L was already introduced in Equation 5 and can be assumed to be a proper velocity scale and assumed to be of the same order of E_L (LaCasce, 2008; Stocchino et al., 2011; Taylor, 1921). Not surprisingly the results suggest that both the nondimensional Lagrangian integral time scale and the dispersion coefficient tend to be constant for the same range of parameters. Moreover, the fact that dispersion tends to be independent in flows where the friction parameter tends to dominate is known also in case of uniform and nonuniform river flows (Besio et al., 2012). The set of Equations 10 and 11–13 could be used to predict the typical dispersion time scales and coefficients especially for weakly and strongly dissipative conditions, which seem to be the most frequent, see Figure 2.

Panel (h) reports the estimated values of the dimensionless diffusion coefficient $K/(E_L T_L)$ as a function of the form factor F. The results suggest that mixed tides enhance the overall longitudinal dispersion with respect to monochromatic tides. In fact, the values of the total nondimensional coefficient show a maximum around $F = 0.5$ and then a slow decrease for increasing F. A second interesting observation regards the effect of the phase lag among the tidal constituents. On average, phase lag $\phi = \pi/4$, namely a lag in the diurnal constituent, produces higher diffusion coefficients. The range of values of $K/(E_L T_L)$ is in agreement with the values obtained for the monochromatic case.

In the end, it is important to understand how the present experimental estimates can be translated to realistic estuaries. Indeed, the observed values of K must be conveniently rescaled in the prototype (an equivalent system with real estuaries dimensions). To this end, let us denote by λ_V and λ_H the scaling factors for velocity and flow depth, respectively defined as the ratio between the typical scale of velocity and flow depth in the prototype and in the laboratory model. Hence, the scaling factor for the dispersive coefficients turn out to be $\lambda_K = \lambda_V^{\frac{1}{2}} \lambda_H$. We are thus able to built λ_K and to rescale the experimental estimates to the reality noting that λ_V can be defined as the ratio between the longitudinal length and time scaling factors, and λ_H belongs from the definition of a typical length scale of estuaries as reported in several works (Seminara et al., 2010; Toffolon et al., 2006; Zhang & Savenije, 2017). The time scaling factor is trivial once we established to represent semi-diurnal or diurnal tides. Depending on the controlling parameters, the present measurements suggest values of K in a range between 10^2 and 10^3 m^2 s^{-1}. Large variability in the diffusion coefficient is commonly observed in field measurements in real estuaries with values comparable with our estimates (Banas et al., 2004; Fischer et al., 1979; Lewis & Uncles, 2003; Monismith et al., 2002). Several authors also report a strong variability of the longitudinal coefficient K_x with the distance from the inlet, with larger values occurring near the ocean (Banas et al., 2004). In order to take into account for this variability, simple scaling has been proposed such as $K_x/(Ub) = c_k$ where U is a scale for the tidal induced velocity, b is the estuary width, and c_k is a constant estimated by a regression over the measurements. Banas et al. (2004) suggested that the constant should assume values in a range between 0.05 and 0.1. This scaling is based on a conceptual model where the major agents of dispersion are thought to be the macro-vortices generated by the residual current (MacCready, 1999) that, as in the present experiments,

scale with the channel width. If we treat the present data using this simple model, we obtain for the constant c_k a median value equal to 0.023 and an estimate of the first percentile (25th) and third percentile (75th) equal to 0.020 and 0.035, respectively, which is fairly closed to the expected value. In real estuaries, this and other similar scaling were suggested in order to take into account for the spatial variability along the estuary. In fact, different mechanisms could modify the value of the longitudinal dispersion coefficient depending on the local hydrodynamics. The proposed relationship based on the external friction parameter should, instead, describe the global response of an estuary without considering a spatial dependency of the coefficient when the hydrodynamic is generated by tidal flow dominated by one harmonic. Finally, a direct comparison with field observations specifically performed to understand the role of the tidal wave shape is complicated by the fact that no information on the typical tides are reported in the studies (Banas et al., 2004; Lewis & Uncles, 2003; Monismith et al., 2002). It would be interesting to verify the tendency of a mixed tide to increase the longitudinal dispersion.

6.3. The Interplay of Flow Structures at Different Scales

The analysis of the Eulerian time-dependent fields shows that even in a relatively simple geometry, as the one used in the present experimental campaign, flow structures at different scales are generated and, more interestingly, they interact within a tidal cycle. The asymptotic dispersion regime proved to exist as an average process over the entire domain. In this section, we are interested to discuss the interplay among the particle trajectories and the different scales of the flow. To this end we apply tools commonly reported as multiple particle statistics, see LaCasce (2008) for a review and application on geophysical contexts.

The computation of $r^2(t)$, D, and $\Lambda(r)$ was performed on both datasets, single and multiple constituents tides, with the aim to understand which are the typical regimes and if different regimes are triggered by more complex forcing. In the case of multiple constituents we again performed a series of simulations varying the initial time of deployment. Figure 7 shows the typical results for the relative dispersion, the dimensionless relative diffusivity coefficient $D/(E_L T_L)$ as a function of the dimensionless separations $r/\left(E_L^{1/2} T_L\right)$, for experiments forced by a single harmonic tide, panels (a) and (b) (experiment 18-SC and experiment 26-SC) and for experiments 4-MC and 13-MC of the multiple components runs, panels (c) and (d). In the same plots the theoretical laws, namely the Richardson-Obukhov and the Kraichnan-Lin laws (Babiano et al., 1990; Bennett, 1984; Er-El & Peskin, 1981; Kraichnan, 1966; Lin, 1972), are shown to help the identification of the regimes.

It is interesting to note that in all cases, regardless the characteristics of the tidal wave, two distinct regimes can be observed. For separation smaller than a typical injection scale $r_i/\left(E_L^{1/2} T_L\right)$, the diffusivity coefficient grows as $D/(E_L T_L) \propto \left(r/\left(E_L^{1/2} T_L\right)\right)^2$, whereas for separation larger than the injection scale the regime follows closely the Richardson-Obukhov law. Correctly for very large separation the growth of the relative diffusivity coefficient attains a constant value $D(E_L T_L) \approx 2\,K/(E_L T_L)$, where $K/(E_L T_L)$ is the total absolute diffusivity, previously defined. The injection scale $r_i/\left(E_L^{1/2} T_L\right)$ is very close to the Lagrangian integral spatial scale. In fact, the change in the relative dispersion regime is close to $r/\left(E_L^{1/2} T_L\right) \approx 1$.

The two-regime scenario is also confirmed by the trends of the dimensionless FSLE ΛT_L as a function of the dimensionless separation $\left(r/\left(E_L^{1/2} T_L\right)\right)$, see panels (e) and (f). As for the autocorrelation functions, grey lines indicate the output for the different deployments, whereas the solid lines represent the averaged value. Also in this case we reported the expected theoretical laws (Artale et al., 1997). The Kraichnan-Lin law previously described is found for $r/\left(E_L^{1/2} T_L\right) < r_i/\left(E_L^{1/2} T_L\right)$ and implies an exponential growth of the FSLEs. As the separation r increases, the FSLE slope suggests the presence of both the Richardson-Obukhov regime $\Lambda T_L \propto \left(r/\left(E_L^{1/2} T_L\right)\right)^{-2/3}$ and the linear regime $\Lambda T_L \propto \left(r/\left(E_L^{1/2} T_L\right)\right)^{-2}$. Moreover, the FSLE for very large separation exhibits the limiting regime expected for separation close to the saturation length r_{max}, that is, the maximum separation imposed by the domain. This is typical for semi-enclosed basins as observed in similar geometrical contexts (Artale et al., 1997; Cencini & Vulpiani, 2013; Enrile et al., 2019).

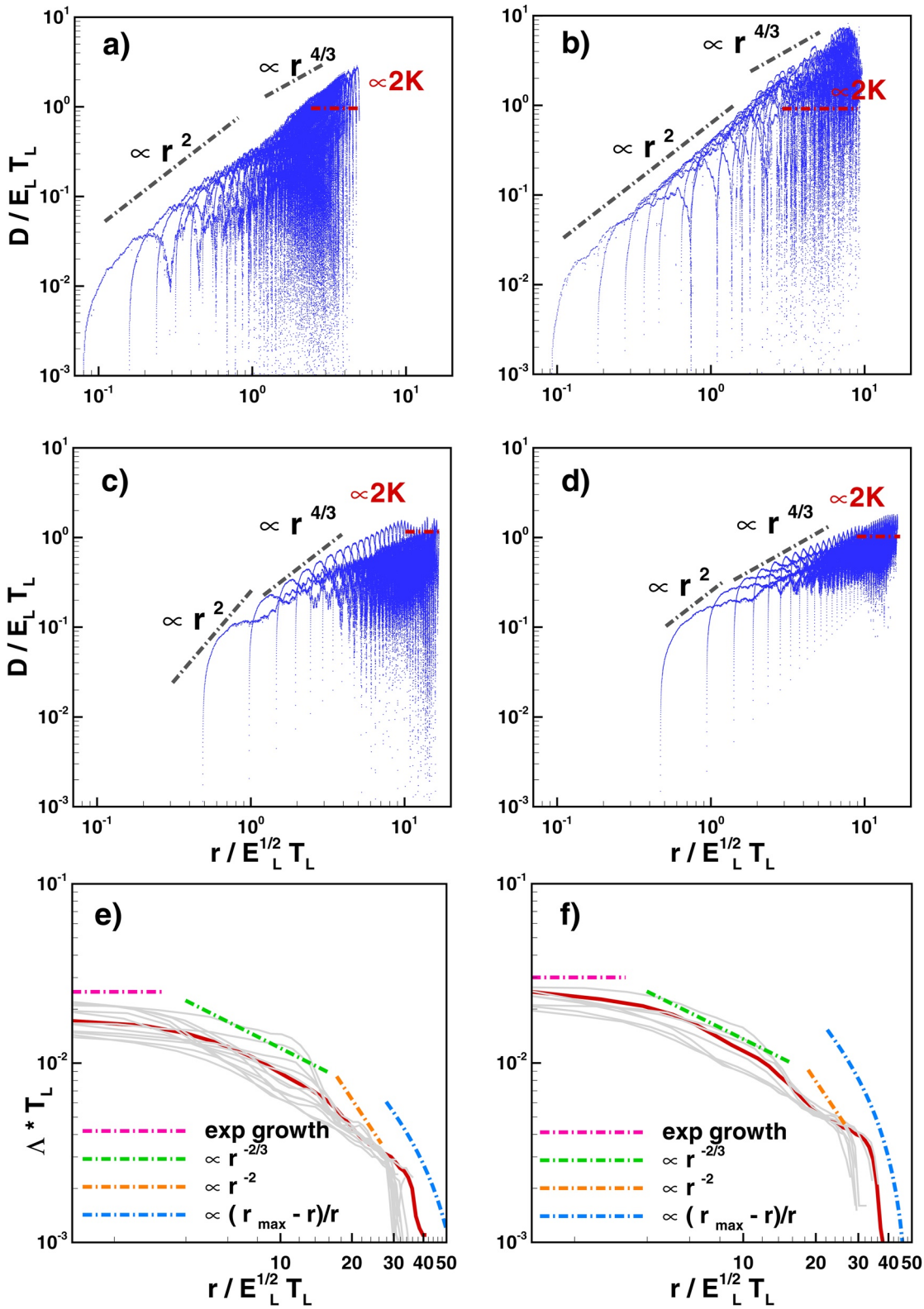

Figure 7. Example of the results obtained from multiple particle statistics analysis. (a) Dimensionless relative dispersion coefficient as a function of the nondimensional separation of experiment 18-SC. (b) Same as panel (a) for experiment 26-SC, (c) experiment 4-MC, and (d) experiment 13-MC; (e) nondimensional FSLE as a function of the nondimensional separation for experiment 4-MC; (f) same as panel (e) for experiment 13-MC. In each panel the expected theoretical laws are also reported.

The results suggest that *local dispersion* is the dominant process for most of the separation range. Relative dispersion in *local dispersion* is characterized by the effect of local straining, which is not efficient in producing large separation, and the dispersion of pairs is dominated by eddies of the same scale of their separation. From a physical standpoint, this could be explained by the presence of large-scale macro-vortices as the dominant features in all tidal cases so that separations are influenced by local straining produced by the mentioned macrovortices.

Moreover, the overall picture seems not to be influenced by tidal wave shape and phase lag between the constituents and this could be explained observing that all the cases are able to trigger similar macro-vortices. Note that the computation of the multiple particle statistics, similarly to the single particle statistics, is averaged over the ensemble of particles deployed uniformly over the domain. This standard procedure relies on the assumption of homogeneity of the flow under investigation (Berloff et al., 2002). Thus, the observed regimes must be considered as the average behavior of the Lagrangian dispersion.

Finally, the injection separation r_i was described as of the same order of magnitude of the Lagrangian integral length scale. However, another length scale could play a role in the present experiments, namely the length of the side wall of the tidal inlet l_i. As previously noted, the generation of the flood-macrovortices is controlled by the vortex shedding from the corners of the tidal inlet. This mechanism could be also explained in analogy with the vortex generation downstream a coastal headland, where the extent of the headland is a controlling length scale of the process (Davies et al., 1995; Signell & Geyer, 1991).

Two observations might be important for the present case. First, the l_i is very close to the Lagrangian integral spatial scale. This could be linked to the nonlinear energy transfer that occurs in a tidal period. In a recent contribution De Leo and Stocchino (2022) demonstrated the occurrence of a multiple energy cascades directly computing the nonlinear energy and enstrophy fluxes, using the same experimental apparatus for a dedicated series of experiments. Moreover, there is a strong relationship between the scaling law of relative dispersion regimes with the energy cascades and transfers (direct/inverse energy cascade and direct/inverse enstrophy cascade). Scaling arguments to describe the different dispersion and energy regimes can be summarized searching for laws of the kind: $D \propto r^{(\alpha+1)/2}$. The link with the energy cascades is the value of the exponent α, having assumed the turbulent energy spectrum as a function of the wave numbers in the form of $E(k) \propto k^{-\alpha}$. Relative dispersion in *local dynamics* is characterized by values $1 < \alpha < 3$ and, in particular, for $\alpha = 5/3$, dispersion of pairs follows the Richardson-Obukhov law that corresponds to the energy cascade $E(k) \propto k^{-5/3}$. On the contrary, *nonlocal dynamics* is characterized by the effect of vortices with typical scales much larger than the separation. This regime is described by the Kraichnan-Lin law $D \propto r^2$, or more generally for $\alpha > 3$. In this case, the expected energy spectrum corresponds to an enstrophy cascade $E(k) \propto k^{-3}$. The change of regimes occurring for a length scale comparable to the Lagrangian spatial scale might suggest a nonlinear energy transfer characterized by an inverse or split energy cascade (Alexakis & Biferale, 2018).

Second, the flow could be described as a forced turbulence, where the forcing is the presence of the tidal inlet and, thus, l_i could be regarded as the length scale of the injected energy. We clearly observed a vortex merging process that several times is a signature of an inverse energy cascade process. A further piece of information that could confirm this scenario is the presence of two distinct regimes in the relative dispersion and in the FSLE, separated by the injection scale r_i. However, further analyses are required to provide a sound proof of the existence of an inverse energy cascade, which would require the evaluation of the energy spectrum and higher order structure functions (Alexakis & Biferale, 2018; Enrile et al., 2020; Nikora et al., 2007).

7. Conclusions

In this study, we reported the results obtained using different tidal forcing on a large-scale physical model of a basin (open ocean) connected to a compound tidal channel through the presence of a barrier island. Large-scale PIV measurements of the 2D free surface time-dependent velocity fields provided a huge data set upon which a thorough Eulerian and Lagrangian analysis was performed. Flood-macrovortices are invariably observed for all experimental parameters. They are clearly generated by interaction between the flow and the inlet mouth. Both experimental series, single and multiple, showed that flood-macrovortices are able to occupy the entire tidal flats. In particular, they are the results of the vortex shedding at the inlet and a merging process that, ultimately, tend to form structures at the scale of the tidal flats width. It was observed that the tidal wave shape, represented by the form factor F in the multi-component series, and the constituent phase lag strongly influence the generation

of the flood-macrovortices in terms of typical length scales. Moreover, the compound geometry seems to sustain the generation of vorticity not only around the inlet, but also along the main channel transition zone (boundary with the tidal flats) forming transient vortical structures. In all cases, the flood-vortices are flushed out during the ebb phase regardless of the Strouhal number. This apparent discrepancy with previous studies (Nicolau del Roure et al., 2009; Wells & van Heijst, 2004) could be ascribed by the role of the compound geometry. Another striking Eulerian flow feature is the generation of an intense residual current, the shape of which is a reminiscence of the transient flood-vortices. Moreover, the residual current seems to be less sensitive to the tidal wave shapes, that is, from the form factor, being very similar among the whole set of experiments.

The flood-macrovortices and the resulting residual currents strongly influence the Lagrangian properties of this class of flows. In particular, Lagrangian auto-correlations are found to oscillate with the dominant tidal period, showing intense negative lobes, soon after the first zero-crossing, leading to super-diffusive regime. More importantly, the nondimensional Lagrangian integral time scale seems to attain a constant value for increasing friction parameter χ, whereas the form factor F has a minor impact on T_L. The same is found for the dispersion coefficients. In fact, on average the total absolute dispersion reached in all cases an asymptotic diffusive regime. The corresponding total diffusivity coefficients K tends to a constant value already for $\chi > 0.15$ in the single component series, whereas K showed a non-monotonic trend with the form factor F. Mixed tides, mainly semi-diurnal ($F > 0.5$), seem to be more efficient for a longitudinal dispersion. We suggested an analytic power law for both the dimensionless integral scale and the dispersive coefficients that might be used to predict the overall dispersion in natural context, which are typically found to be in a strong dissipative regime.

Regarding the multiple particle dispersion processes, both the regimes in the total relative diffusion coefficient and the FSLEs show that the flow is dominated by two regimes for separations lower or greater of a typical injection scale, which seems to be equal to the Lagrangian integral length scale of the lateral extension of the tidal inlet, regardless of the series considered. The Richardson regime of *local dynamics* dominates for a wide range of separation larger than r_i and smaller of a saturation length highlighted in the FSLE trends. Tidal flows are governed by large macro-vortices larger than the mean separation.

The present experiments provide a deep understanding of the main dispersion processes occurring in weakly-dissipative tidal systems characterized by the presence of a tidal inlet. We acknowledge that the present experimental setup had some important limitations, such as the absence of river inputs and stratification effects. Future activities will be devoted to overcome the latter limitations changing the experimental conditions.

Conflict of Interest

The authors declare no conflicts of interest relevant to this study.

Data Availability Statement

Data management repository available at doi: https://doi.org/10.5281/zenodo.5751878.

Acknowledgments
This research has not been supported by external funding. Open Access Funding provided by Università degli Studi di Genova within the CRUI-CARE Agreement.

References

Alexakis, A., & Biferale, L. (2018). Cascades and transitions in turbulent flows. *Physics Reports*, *767*, 1–101. https://doi.org/10.1016/j.physrep.2018.08.001

Alosairi, Y., & Alsulaiman, N. (2019). Hydro-environmental processes governing the formation of hypoxic parcels in an inverse estuarine water body: Model validation and discussion. *Marine Pollution Bulletin*, *144*, 92–104. https://doi.org/10.1016/j.marpolbul.2019.04.067

Amin, M. (1986). On the conditions for classification of tides. *International Hydrographic Review*, *63*, 1. Retrieved from https://journals.lib.unb.ca/index.php/ihr/article/view/23443

Artale, V., Boffetta, G., Celani, A., Cencini, M., & Vulpiani, A. (1997). Dispersion of passive tracers in closed basins: Beyond the diffusion coefficient. *Physics of Fluids*, *9*(11), 3162–3171. https://doi.org/10.1063/1.869433

Aubrey, D., & Speer, P. (1985). A study of non-linear tidal propagation in shallow inlet/estuarine systems Part I: Observations. *Estuarine, Coastal and Shelf Science*, *21*(2), 185–205. https://doi.org/10.1016/0272-7714(85)90096-4

Awaji, T. (1982). Water mixing in a tidal current and the effect of turbulence on tidal exchange through a strait. *Journal of Physical Oceanography*, *12*(6), 501–514. https://doi.org/10.1175/1520-0485(1982)012<0501:wmiatc>2.0.co;2

Awaji, T., Imasato, N., & Kunishi, H. (1980). Tidal exchange through a strait: A numerical experiment using a simple model basin. *Journal of Physical Oceanography*, *10*(10), 1499–1508. https://doi.org/10.1175/1520-0485(1980)010<1499:tetasa>2.0.co;2

Babiano, A., Basdevant, C., Le Roy, P., & Sadourny, R. (1990). Relative dispersion in two-dimensional turbulence. *Journal of Fluid Mechanics*, *214*, 535–557. https://doi.org/10.1017/s0022112090000258

Banas, N., Hickey, B., MacCready, P., & Newton, J. (2004). Dynamics of Willapa Bay, Washington: A highly unsteady, partially mixed estuary. *Journal of Physical Oceanography*, *34*(11), 2413–2427. https://doi.org/10.1175/jpo2637.1
Beerens, S., Ridderinkhof, H., & Zimmerman, J. (1994). An analytical study of chaotic stirring in tidal areas. *Chaos, Solitons & Fractals*, *4*(6), 1011–1029. https://doi.org/10.1016/0960-0779(94)90136-8
Bennett, A. (1984). Relative dispersion: Local and nonlocal dynamics. *Journal of Atmospheric Sciences*, *41*, 1881–1886. https://doi.org/10.1175/1520-0469(1984)041<1881:rdland>2.0.co;2
Berloff, P. S., McWilliams, J. C., & Bracco, A. (2002). Material transport in oceanic gyres. Part I: Phenomenology. *Journal of Physical Oceanography*, *32*(3), 764–796. https://doi.org/10.1175/1520-0485(2002)032<0764:mtiogp>2.0.co;2
Besio, G., Stocchino, A., Angiolani, S., & Brocchini, M. (2012). Transversal and longitudinal mixing in compound channels. *Water Resources Research*, *48*(12). https://doi.org/10.1029/2012wr012316
Blondeaux, P., & Vittori, G. (2020). Modeling transverse coastal bedforms at Anna Maria Island (Florida). *Journal of Geophysical Research: Oceans*, *125*(7), e2019JC015837. https://doi.org/10.1029/2019jc015837
Branyon, J., Valle-Levinson, A., Mariño-Tapia, I., & Enriquez, C. (2022). Intratidal and residual flows around inlets of a reef lagoon. *Estuaries and Coasts*, *45*, 63–77. https://doi.org/10.1007/s12237-021-00940-3
Brocchini, M., & Colombini, M. (2004). A note on the decay of vorticity in shallow flow calculations. *Physics of Fluids*, *16*(7), 2469–2475. https://doi.org/10.1063/1.1756551
Cai, H., Savenije, H. H., & Toffolon, M. (2012). A new analytical framework for assessing the effect of sea-level rise and dredging on tidal damping in estuaries. *Journal of Geophysical Research*, *117*(C9). https://doi.org/10.1029/2012jc008000
Cencini, M., & Vulpiani, A. (2013). Finite size Lyapunov exponent: Review on applications. *Journal of Physics A: Mathematical and Theoretical*, *46*(25), 254019. https://doi.org/10.1088/1751-8113/46/25/254019
Chau, K. W. (2000). Transverse mixing coefficient measurements in an open rectangular channel. *Advances in Environmental Research*, *4*(4), 287–294. https://doi.org/10.1016/s1093-0191(00)00028-9
Cucco, A., Umgiesser, G., Ferrarin, C., Perilli, A., Canu, D. M., & Solidoro, C. (2009). Eulerian and Lagrangian transport time scales of a tidal active coastal basin. *Ecological Modelling*, *220*(7), 913–922. https://doi.org/10.1016/j.ecolmodel.2009.01.008
Davies, P. A., Dakin, J. M., & Falconer, R. A. (1995). Eddy formation behind a coastal headland. *Journal of Coastal Research*, *11*(1), 154–167.
Davis, R., & Moore, E. (1982). A numerical study of vortex shedding from rectangles. *Journal of Fluid Mechanics*, *116*, 475–506. https://doi.org/10.1017/s0022112082000561
De Leo, A., & Stocchino, A. (2022). Evidence of transient energy and enstrophy cascades in tidal flows: A scale to scale analysis. *Geophysical Research Letters*, *49*(10), e2022GL098043. https://doi.org/10.1029/2022gl098043
Dronkers. (2019). Estuarine dispersion: Dye experiments in the Eastern Scheldt scale model. http://www.coastalwiki.org/wiki/
Elhmaïdi, D., Provenzale, A., & Babiano, A. (1993). Elementary topology of two-dimensional turbulence from a Lagrangian viewpoint and single-particle dispersion. *Journal of Fluid Mechanics*, *257*, 533–558. https://doi.org/10.1017/s0022112093003192
Enrile, F., Besio, G., & Stocchino, A. (2018). Shear and shearless Lagrangian structures in compound channels. *Advances in Water Resources*, *113*, 141–154. https://doi.org/10.1016/j.advwatres.2018.01.006
Enrile, F., Besio, G., & Stocchino, A. (2020). Eulerian spectrum of finite-time Lyapunov exponents in compound channels. *Meccanica*, *55*(9), 1821–1828. https://doi.org/10.1007/s11012-020-01217-y
Enrile, F., Besio, G., Stocchino, A., Magaldi, M., Mantovani, C., Cosoli, S., et al. (2018). Evaluation of surface Lagrangian transport barriers in the Gulf of Trieste. *Continental Shelf Research*, *167*, 125–138. https://doi.org/10.1016/j.csr.2018.04.016
Enrile, F., Besio, G., Stocchino, A., & Magaldi, M. G. (2019). Influence of initial conditions on absolute and relative dispersion in semi-enclosed basins. *PLoS One*, *14*(7), e0217073. https://doi.org/10.1371/journal.pone.0217073
Er-El, J., & Peskin, R. (1981). Relative diffusion of constant-level balloons in the Southern hemisphere. *Journal of Atmospheric Sciences*, *38*(10), 2264–2274. https://doi.org/10.1175/1520-0469(1981)038<2264:rdoclb>2.0.co;2
Fischer, H. B., List, J. E., Koh, C. R., Imberger, J., & Brooks, N. H. (1979). *Mixing in inland and coastal waters*. Academic Press.
Fortunato, A. B., & Oliveira, A. (2005). Influence of intertidal flats on tidal asymmetry. *Journal of Coastal Research*, *21*(5), 1062–1067. https://doi.org/10.2112/03-0089.1
Friedrichs, C. T., & Madsen, O. S. (1992). Nonlinear diffusion of the tidal signal in frictionally dominated embayments. *Journal of Geophysical Research*, *97*(C4), 5637–5650. https://doi.org/10.1029/92jc00354
Geng, L., Gong, Z., Zhou, Z., Lanzoni, S., & D'Alpaos, A. (2020). Assessing the relative contributions of the flood tide and the ebb tide to tidal channel network dynamics. *Earth Surface Processes and Landforms*, *45*(1), 237–250. https://doi.org/10.1002/esp.4727
Geyer, W. R., & MacCready, P. (2014). The estuarine circulation. *Annual Review of Fluid Mechanics*, *46*, 175–197. https://doi.org/10.1146/annurev-fluid-010313-141302
Gisen, J. I. A., & Savenije, H. H. (2015). Estimating bankfull discharge and depth in ungauged estuaries. *Water Resources Research*, *51*(4), 2298–2316. https://doi.org/10.1002/2014wr016227
Haza, A. C., Poje, A. C., Özgökmen, T. M., & Martin, P. (2008). Relative dispersion from a high-resolution coastal model of the Adriatic Sea. *Ocean Modelling*, *22*(1–2), 48–65. https://doi.org/10.1016/j.ocemod.2008.01.006
Jay, D. A. (1991). Green's law revisited: Tidal long-wave propagation in channels with strong topography. *Journal of Geophysical Research*, *96*(C11), 20585–20598. https://doi.org/10.1029/91jc01633
Jirka, G. (2001). Large scale flow structures and mixing processes in shallow flows. *Journal of Hydraulic Research*, *39*, 567–573. https://doi.org/10.1080/00221686.2001.9628285
Kang, J., & Jun, K. (2003). Flood and ebb dominance in estuaries in Korea. *Estuarine, Coastal and Shelf Science*, *56*(1), 187–196. https://doi.org/10.1016/s0272-7714(02)00156-7
Kraichnan, H. (1966). Dispersion of particle pairs in homogeneous turbulence. *Physics of Fluids*, *9*, 1937–1943. https://doi.org/10.1063/1.1761547
Kusumoto. (2008). Laboratory experiments of tidal dispersion around irregular boundaries (Phd thesis).
LaCasce, J. (2008). Statistics from Lagrangian observations. *Progress in Oceanography*, *77*, 1–29. https://doi.org/10.1016/j.pocean.2008.02.002
Lanzoni, S., & Seminara, G. (1998). On tide propagation in convergent estuaries. *Journal of Geophysical Research*, *103*(C13), 30793–30812. https://doi.org/10.1029/1998jc900015
Lee, S.-H., & Chang, Y.-S. (2019). Classification of the global tidal types based on auto-correlation analysis. *Ocean Science Journal*, *54*(2), 279–286. https://doi.org/10.1007/s12601-019-0009-7
Lewis, R. E., & Uncles, R. J. (2003). Factors affecting longitudinal dispersion in estuaries of different scale. *Ocean Dynamics*, *53*(3), 197–207. https://doi.org/10.1007/s10236-003-0030-2
Lin, J. (1972). Relative dispersion in the enstrophy cascading inertial range of homogeneous two dimensional turbulence. *Journal of the Atmospheric Sciences*, *29*, 394–396. https://doi.org/10.1175/1520-0469(1972)029<0394:rditec>2.0.co;2

MacCready, P. (1999). Estuarine adjustment to changes in river flow and tidal mixing. *Journal of Physical Oceanography*, *29*(4), 708–726. https://doi.org/10.1175/1520-0485(1999)029<0708:eatcir>2.0.co;2

Monismith, S. G., Kimmerer, W., Burau, J. R., & Stacey, M. T. (2002). Structure and flow-induced variability of the subtidal salinity field in northern San Francisco Bay. *Journal of Physical Oceanography*, *32*(11), 3003–3019. https://doi.org/10.1175/1520-0485(2002)032<3003:safivo>2.0.co;2

Nezu, I., Onitsuka, K., & Iketani, K. (1999). Coherent horizontal vortices in compound open-channel flows. *Hydraulic Modeling*, 17–32.

Nicolau del Roure, F., Socolofsky, S. A., & Chang, K.-A. (2009). Structure and evolution of tidal starting jet vortices at idealized barotropic inlets. *Journal of Geophysical Research*, *114*(C5). https://doi.org/10.1029/2008jc004997

Nikora, V., Nokes, R., Veale, W., Davidson, M., & Jirka, G. (2007). Large-scale turbulent structure of uniform shallow free-surface flows. *Environmental Fluid Mechanics*, *7*, 159–172. https://doi.org/10.1007/s10652-007-9021-z

Okubo, A. (1970). Horizontal dispersion of floatable particles in the vicinity of velocity singularities such as convergences. *Deep Sea Research and Oceanographic Abstracts*, *17*, 445–454. https://doi.org/10.1016/0011-7471(70)90059-8

Orre, S., Gjevik, B., & LaCasce, J. H. (2006). Characterizing chaotic dispersion in a coastal tidal model. *Continental Shelf Research*, *26*(12–13), 1360–1374. https://doi.org/10.1016/j.csr.2005.11.015

Provenzale, A. (1999). Transport by coherent barotropic vortices. *Annual Review of Fluid Mechanics*, *31*, 55–93. https://doi.org/10.1146/annurev.fluid.31.1.55

Ren, Y., Lin, B., Sun, J., & Pan, S. (2014). Predicting water age distribution in the Pearl River Estuary using a three-dimensional model. *Journal of Marine Systems*, *139*, 276–287. https://doi.org/10.1016/j.jmarsys.2014.07.005

Ridderinkhof, H., & Zimmerman, J. (1992). Chaotic stirring in a tidal system. *Science*, *258*(5085), 1107–1111. https://doi.org/10.1126/science.258.5085.1107

Savenije, H. H. (1993). Determination of estuary parameters on basis of Lagrangian analysis. *Journal of Hydraulic Engineering*, *119*(5), 628–642. https://doi.org/10.1061/(asce)0733-9429(1993)119:5(628)

Seminara, G., Lanzoni, S., Tambroni, N., & Toffolon, M. (2010). How long are tidal channels? *Journal of Fluid Mechanics*, *643*, 479. https://doi.org/10.1017/s0022112009992308

Shiono, K., & Knight, D. (1991). Turbulent open-channel flows with variable depth across the channel. *Journal of Fluid Mechanics*, *222*, 617–646. https://doi.org/10.1017/s0022112091001246

Signell, R. P., & Geyer, W. R. (1991). Transient eddy formation around headlands. *Journal of Geophysical Research*, *96*(C2), 2561–2575. https://doi.org/10.1029/90jc02029

Stocchino, A., Besio, G., Angiolani, S., & Brocchini, M. (2011). Lagrangian mixing in straight compound channels. *Journal of Fluid Mechanics*, *675*, 168. https://doi.org/10.1017/s0022112011000127

Stocchino, A., & Brocchini, M. (2010). Horizontal mixing of quasi-uniform, straight, compound channel flows. *Journal of Fluid Mechanics*, *643*, 425–435. https://doi.org/10.1017/s0022112009992680

Sumer, B. M. (2006). *Hydrodynamics around cylindrical structures (Vol. 26)*. World Scientific.

Taylor, G. (1921). Diffusion by continuous movement. *Proceedings of the London Mathematical Society*, *20*, 196–212.

Toffolon, M., Vignoli, G., & Tubino, M. (2006). Relevant parameters and finite amplitude effects in estuarine hydrodynamics. *Journal of Geophysical Research*, *111*(C10). https://doi.org/10.1029/2005jc003104

Tsimplis, M., Proctor, R., & Flather, R. (1995). A two-dimensional tidal model for the Mediterranean Sea. *Journal of Geophysical Research*, *100*(C8), 16223–16239. https://doi.org/10.1029/95jc01671

Umgiesser, G., Ferrarin, C., Cucco, A., De Pascalis, F., Bellafiore, D., Ghezzo, M., & Bajo, M. (2014). Comparative hydrodynamics of 10 Mediterranean lagoons by means of numerical modeling. *Journal of Geophysical Research: Oceans*, *119*(4), 2212–2226. https://doi.org/10.1002/2013jc009512

Valle-Levinson, A. (2010). *Contemporary issues in estuarine physics*. Cambridge University Press.

Valle-Levinson, A. (2021). Dynamics-based classification of semienclosed basins. *Regional Studies in Marine Science*, *46*,101866. https://doi.org/10.1016/j.rsma.2021.101866

Van Prooijen, B. C., Battjes, J. A., & Uijttewaal, W. S. (2005). Momentum exchange in straight uniform compound channel flow. *Journal of Hydraulic Engineering*, *131*(3), 175–183. https://doi.org/10.1061/(asce)0733-9429(2005)131:3(175)

Veneziani, M., Griffa, A., Reynolds, A. M., & Mariano, A. J. (2004). Oceanic turbulence and stochastic models from subsurface Lagrangian data for the northwest Atlantic Ocean. *Journal of Physical Oceanography*, *34*(8), 1884–1906. https://doi.org/10.1175/1520-0485(2004)034<1884:otasmf>2.0.co;2

Viero, D. P., & Defina, A. (2016). Water age, exposure time, and local flushing time in semi-enclosed, tidal basins with negligible freshwater inflow. *Journal of Marine Systems*, *156*, 16–29. https://doi.org/10.1016/j.jmarsys.2015.11.006

Vouriot, C. V., Angeloudis, A., Kramer, S. C., & Piggott, M. D. (2019). Fate of large-scale vortices in idealized tidal lagoons. *Environmental Fluid Mechanics*, *19*(2), 329–348. https://doi.org/10.1007/s10652-018-9626-4

Webel, G., & Schatzmann, M. (1984). Transverse mixing in open channel flow. *Journal of Hydraulic Engineering*, *110*(4), 423–435. https://doi.org/10.1061/(asce)0733-9429(1984)110:4(423)

Weiss, J. (1991). The dynamics of enstrophy transfer in two-dimensional hydrodynamics. *Physica D*, *48*, 272–294. https://doi.org/10.1016/0167-2789(91)90088-q

Wells, M., & van Heijst, G. (2004). Dipole formation by tidal flow in a channel. In *International symposium on shallow flows* (pp. 63–70). Balkema Publishers.

Yang, Y., Chui, T. F. M., Shen, P. P., Yang, Y., & Gu, J. D. (2018). Modeling the temporal dynamics of intertidal benthic infauna biomass with environmental factors: Impact assessment of land reclamation. *Science of the Total Environment*, *618*, 439–450. https://doi.org/10.1016/j.scitotenv.2017.10.325

Zhang, Z., & Savenije, H. H. (2017). The physics behind van der Burgh's empirical equation, providing a new predictive equation for salinity intrusion in estuaries. *Hydrology and Earth System Sciences*, *21*(7), 3287–3305. https://doi.org/10.5194/hess-21-3287-2017

Zimmerman, J. (1986). The tidal whirlpool: A review of horizontal dispersion by tidal and residual currents. *Netherlands Journal of Sea Research*, *20*(2–3), 133–154. https://doi.org/10.1016/0077-7579(86)90037-2